

1 **Potential Influences of Neglecting Aerosol Effects on the NCEP**

2 **GFS Precipitation Forecast**

3
4 Mengjiao Jiang^{1,2}, Jinqin Feng³, Zhanqing Li^{1,2*}, Ruiyu Sun⁴, Yu-Tai Hou⁴, Yuejian

5 Zhu⁴, Bingcheng Wan⁵, Jianping Guo⁶, Maureen Cribb²

6
7 1, State Key Laboratory of Earth Surface Processes and Resource Ecology, College of
8 Global Change and Earth System Science, Beijing Normal University, Beijing, China

9 2, Department of Atmospheric and Oceanic Science and ESSIC, University of
10 Maryland, College Park, Maryland, USA

11 3, Longyan Meteorological Office of Fujian Province, Longyan, Fujian, China

12 4, Environmental Modeling Center, National Centers for Environmental Prediction,
13 National Oceanic and Atmospheric Administration, USA

14 5, State Key Laboratory of Atmospheric Boundary Layer Physics and Atmospheric
15 Chemistry, Institute of Atmospheric Physics, Chinese Academy of Sciences, Beijing,
16 China

17 6, State Key Laboratory of Severe Weather, Chinese Academy of Meteorological
18 Sciences, Beijing, China

19
20 Correspondence to:

21 Z. Li,

22 zhanqing@umd.edu

23 **Abstract**

24 Aerosol-cloud interactions (ACI) have been widely recognized as a factor affecting
25 precipitation. However, they have not been considered in the operational National
26 Centers for Environmental Predictions Global Forecast System model. We evaluated
27 the potential impact of neglecting ACI on the operational rainfall forecast using
28 ground-based and satellite observations, and model reanalysis. The Climate Prediction
29 Center unified gauge-based precipitation analysis and the Modern-Era Retrospective
30 analysis for Research and Applications Version 2 aerosol reanalysis were used to
31 evaluate the forecast in three countries for the year 2015. The overestimation of light
32 rain (47.84%) and underestimation of heavier rain (31.83%, 52.94%, and 65.74% for
33 moderate rain, heavy rain, and very heavy rain, respectively) from the model are
34 qualitatively consistent with the potential errors arising from not accounting for ACI,
35 although other factors cannot be totally ruled out. The standard deviation of the
36 forecast bias was significantly correlated with aerosol optical depth in Australia, the
37 U.S., and China. To gain further insight, we chose the province of Fujian in China to
38 pursue a more insightful investigation using a suite of variables from gauge-based
39 observations of precipitation, visibility, water vapor, convective available potential
40 energy (CAPE), and satellite datasets. Similar forecast biases were found:
41 over-forecasted light rain and under-forecasted heavy rain. Long-term analyses
42 revealed an increasing trend of heavy rain in summer, and a decreasing trend of light
43 rain in other seasons, accompanied by a decreasing trend in visibility, no trend in
44 water vapor, and a slight increasing trend in summertime CAPE. More aerosols

45 decreased cloud effective radii for cases where the liquid water path was greater than
46 100 g m^{-2} . All findings are consistent with the effects of ACI, i.e., where aerosols
47 inhibit the development of shallow liquid clouds and invigorate warm-base
48 mixed-phase clouds (especially in summertime), which in turn affects precipitation.
49 While we cannot establish rigorous causal relations based on the analyses presented in
50 this study, the significant rainfall forecast bias seen in operational weather forecast
51 model simulations warrants consideration in future model improvements.

52 **1. Introduction**

53 Aerosols affect precipitation by acting as cloud condensation nuclei (CCN) and
54 ice nuclei (IN), which can influence cloud microphysics (Twomey et al., 1984) and
55 cloud lifetime (Albrecht, 1989). By absorbing and scattering radiation in the
56 atmosphere, aerosols can alter the thermal and dynamic conditions of the atmosphere.
57 The two types of effects are broadly referred to as aerosol-cloud interactions (ACI)
58 and aerosol-radiation interactions (ARI) (Intergovernmental Panel on Climate Change,
59 2013). Both can influence precipitation (Rosenfeld et al., 2008) and many other
60 meteorological variables to the extent that they may account for the considerable
61 changes in climate experienced in Asia over the past half century (Li et al., 2016).

62 The impact of aerosols on precipitation via cloud microphysics occurs through
63 warm-rain and cold-rain processes, as reviewed by Tao et al. (2012). In the warm-rain
64 process, the competition for water vapor leads to a greater number of cloud drops with
65 smaller sizes as the aerosol loading increases. This decreases the collision efficiency
66 because of the low fall speed and low droplet-collecting efficiency. Rain formation is
67 thus slowed down. Also, a heavier aerosol loading narrows the cloud drop-size
68 spectrum, lowering the coalescence and collision efficiencies. The delay in
69 precipitation formation from the warm-rain process enhances condensation and
70 freezing, and ultimately, leads to the release of extra latent heat above the 0°C
71 isotherm (Andreae et al., 2004; Rosenfeld et al., 2008), favoring mixed-phase and
72 cold rainfall processes. ARI also affect precipitation. First, solar radiation absorbed by
73 aerosols may warm up a cloud droplet enough to evaporate it (Ackerman et al., 2000).

74 Second, heating of an aerosol layer due to absorption and cooling of the surface
75 because of the reduction in radiation reaching the ground stabilizes the lower
76 boundary-layer atmosphere and suppresses the formation and development of low
77 clouds whose occurrence decreases with increasing aerosol loading (Li et al., 2011).
78 The suppressed convection by ARI may also lead to rainfall enhancement downwind
79 of polluted places (Carrió et al., 2010; Fan et al., 2015). The combination of ARI and
80 ACI leads to a non-monotonic response of rainfall to aerosols: increasing first and
81 then decreasing (Jiang et al., 2016) because the ACI and ARI are most significant for
82 low and high aerosol loadings, respectively (Rosenfeld et al., 2008; Koren et al., 2008;
83 Fan et al., 2016).

84 Most findings concerning the aerosol suppression of clouds and precipitation are
85 associated with stratocumulus clouds, cumulus clouds, and shallow convection
86 (Albrecht, 1989; Rosenfeld, 2000; Jiang et al., 2006; Xue & Feingold, 2006; Khain et
87 al., 2008), whereas those of enhanced rainfall are associated with deep convective
88 clouds (Koren et al., 2005; Lin et al., 2006; Bell et al., 2008; Rosenfeld et al., 2008).
89 Li et al. (2011) used 10 years of ground-based observations to examine the long-term
90 impact of aerosols on precipitation and found rainfall enhancement in mixed-phase
91 warm-base clouds and suppression in liquid clouds. Van den Heever et al. (2011)
92 underlined the importance of cloud type in dealing with the impact of aerosols on
93 precipitation.

94 Forecasting rainfall is most challenging and important in numerical weather
95 prediction (NWP). In the current Global Forecast System (GFS) model, aerosols are

196 only considered in the radiation scheme on a climatological scale. ARI are only
197 considered offline and are not coupled with the dynamic system. ACI have not yet
198 been accounted for. To improve the forecast accuracy, a suite of new physical schemes
199 are being implemented in the National Centers for Environmental Prediction
200 (NCEP)'s Next-Generation Global Prediction System. The goal of modifying the
201 current forecast model is to improve physical parameterizations in such a way that
202 allows for efficient, accurate, and more complete representations of physical
203 processes and their interactions including at least some of the aforementioned aerosol
204 mechanisms.

205 As a first step, the goal of the present study is to evaluate current operational
206 GFS forecast results (before any ACI are introduced) to see if any systematic
207 precipitation biases bear resemblance to aerosol perturbations. A gross evaluation of
208 the GFS model forecast results in three countries (China, the U.S., and Australia) were
209 chosen because they cover all hemispheres and represent different atmospheric and
210 environmental conditions. Moreover, there are the U.S. Department of Energy's
211 Atmospheric Radiation Measurement (ARM) observations in all three countries that
212 will be used in follow-on studies to gain a deeper insight into causal relationships and
213 the impact of different parameterization schemes. Descriptions of the operational GFS
214 model, datasets, and the evaluation strategy and statistical method used are presented
215 in section 2. Results of the evaluation and possible explanations are given in section 3.
216 A summary of the research and discussion are given in Section 4.

217

118 2. Model, Datasets, and Methodology

119

120 2.1 Description of the NCEP GFS Model

121 The NCEP GFS model is a global spectral forecast model (spherical harmonic
122 basis functions) that has been described and evaluated over the years (e.g., Kanamitsu,
123 1989; Yang et al., 2006; Sela, 2009; Yoo et al., 2012, 2013). Shortwave and longwave
124 radiation are parameterized using the Rapid Radiative Transfer Models (RRTMG)
125 RRTMG_SW (v3.8) and RRTMG_LW (updated based on AER's version 4.8),
126 respectively, developed at AER Inc. (<http://www.emc.ncep.noaa.gov/GFS/doc.php>). A
127 monthly climatology of aerosols composed of five primary species similar to those in
128 the Goddard Chemistry Aerosol Radiation and Transport model (GOCART; Chin et
129 al., 2002) was used. **One or two major components in each grid (based on climatology)**
130 **were chosen for both longwave and shortwave radiative transfer calculations.** In the
131 planetary boundary layer (PBL), a hybrid eddy-diffusivity mass flux PBL
132 parameterization (Han et al., 2016) was incorporated to replace the previous PBL
133 scheme (Troen & Mahrt, 1986; Hong & Pan, 1996). A modified version (Han & Pan,
134 2011) of the Simplified Arakawa-Schubert scheme (Arakawa & Schubert, 1974; Grell,
135 1993; Pan & Wu, 1995) is used for deep convection in the GFS model. The new
136 shallow convection scheme (Han & Pan, 2011) uses a bulk mass-flux
137 parameterization, which is similar to the deep convection scheme, but with a
138 cloud-top limit of 700 hPa and different specifications on entrainment, detrainment,
139 and mass flux at the cloud base. A prognostic cloud water scheme (Sundqvist et al.,

140 1989; Zhao & Carr, 1997; Moorthi et al., 2001) was added in May 2001. Grid-scale
141 precipitation is the sink of cloud condensate and is diagnostically calculated from
142 cloud condensate. It is parameterized following Zhao & Carr (1997) for ice (snow),
143 evaporation of rain and snow, and the melting of snow, and following Sundvist et al.
144 (1989) for liquid water (rain) (GCWM Branch, EMC, 2003).

145

146 **2.2 Descriptions of Datasets Used**

147 Datasets used include Modern-Era Retrospective analysis for Research and
148 Applications Version 2 (MERRA-2) aerosol optical depth (AOD) data, Climate
149 Prediction Center (CPC) unified gauge-based precipitation data, and the NCEP GFS
150 precipitation forecast data for the year 2015 in three countries: China, the U.S., and
151 Australia. Other datasets used include long-term NCEP Global Ensemble Forecast
152 System (GEFS) precipitation forecast data, ground-based observations of precipitation
153 and visibility, water vapor and convective available potential energy (CAPE)
154 sounding datasets, and satellite-retrieved aerosol and cloud properties for a small
155 region of Fujian Province in China chosen for more detailed study.

156 **2.2.1 NASA MERRA-2 Aerosol Reanalysis**

157 The MERRA-2 aerosol reanalysis (Randles et al., 2016) is an upgrade of the
158 off-line aerosol reanalysis called MERRAero (da Silva et al., 2011; Rienecker et al.,
159 2011; Jiang et al., 2016). The aerosol module in MERRAero is based on the
160 GOCART model (Chin et al., 2002). The AOD observing system sensors extend from
161 the Moderate Resolution Imaging Spectroradiometer (MODIS) Neural Net Retrieval

162 (NNR) in MERRAero to a combination of the Advanced Very-High-Resolution
163 Radiometer NNR, Aerosol Robotic Network, the Multi-angle Imaging
164 SpectroRadiometer, the MODIS/Terra NNR, and the MODIS/Aqua NNR in the
165 MERRA-2 aerosol reanalysis. More details about the MERRA-2 aerosol reanalysis
166 can be found in Randles et al. (2016). Hourly total aerosol extinction AOD data at 550
167 nm at a resolution of $0.625^\circ \times 0.5^\circ$ for the year 2015 are used in this study.

168 **2.2.2 CPC Unified Gauge-based Analysis of Global Daily Precipitation**

169 A unified suite of precipitation analysis products that ingest a gauge-based
170 analysis of global daily precipitation over land were assembled at NOAA's CPC
171 ([https://climatedataguide.ucar.edu/climate-data/cpc-unified-gauge-based-analysis-glob](https://climatedataguide.ucar.edu/climate-data/cpc-unified-gauge-based-analysis-global-daily-precipitation)
172 [al-daily-precipitation](https://climatedataguide.ucar.edu/climate-data/cpc-unified-gauge-based-analysis-global-daily-precipitation)). Over 17,000 station reports were first collected from multiple
173 sources. Quality control was performed through comparisons with other sources of
174 data, e.g., from radar, satellite, numerical models, independent nearby stations, and
175 historical precipitation records. Post-quality control corrected reports are interpolated
176 to create the analyzed fields. Orographic effects are considered in this step (Xie et al.,
177 2007). Finally, the daily analysis is constructed and released at a $0.5^\circ \times 0.5^\circ$ resolution
178 ([https://climatedataguide.ucar.edu/climate-data/cpc-unified-gauge-based-analysis-glob](https://climatedataguide.ucar.edu/climate-data/cpc-unified-gauge-based-analysis-global-daily-precipitation)
179 [al-daily-precipitation](https://climatedataguide.ucar.edu/climate-data/cpc-unified-gauge-based-analysis-global-daily-precipitation)). Daily precipitation data for the year 2015 are used in this
180 study.

181 **2.2.3 NCEP GFS/GEFS Forecast Datasets**

182 NWP model forecast data used are three-hourly rainfall forecasts from the NCEP
183 GFS model initialized at 00 coordinated universal time (UTC) and accumulated for 24

184 hours in the three countries chosen for study. The relative humidity (RH) at 850 hPa
185 and the liquid water path (LWP) calculated following Yoo et al. (2012) are used,
186 corresponding to the precipitation record in the three countries at a 0.5°x0.5°
187 latitude-longitude resolution. For the part of the study focused on Fujian Province,
188 China, the long-term NWP model reforecast precipitation amount accumulated over
189 the period of 12 hours to 36 hours out from 00 UTC at a 1°x1° latitude-longitude
190 resolution for the years 1985 to 2010 are used.

191 **2.2.4 Long-term Ground-based Observations in Fujian Province, China**

192 Ground meteorological data acquired in Fujian Province from 1980 to 2009 are
193 used in this study. Figure 1 shows the locations of the 67 meteorological stations
194 measuring precipitation. Sixteen of these stations also collect visibility data four times
195 a day. Daily mean data are used here. Visibility has been used as proxy for aerosol
196 loading in China in several studies (Rosenfeld et al., 2007; Yang et al., 2013; Yang &
197 Li, 2014). The main advantage is the long measurement record under all sky
198 conditions. However, there are some limitations, e.g., the uncertainty due to humans
199 making the observations and the influence of aerosol hygroscopic growth. To remove
200 the humidity influence on visibility, visibility was corrected for RH (Charlson, 1969;
201 Appel et al., 1985) using the formula adopted by Rosenfeld et al. (2007) when RH
202 falls between 40% and 99%:

$$203 \quad \frac{V_{ori}}{V_{cor}} = 0.26 + 0.4285 \lg(100 - RH), \quad (1)$$

204 where RH is in percent, and V_{ori} and V_{cor} are the originally uncorrected and
205 corrected visibilities, respectively. Only non-rainy data were used.

206 To analyze water vapor and atmospheric stability effects on precipitation, **data**
207 **collected twice a day (at 00 UTC and 12 UTC) from three atmospheric sounding**
208 stations (Xiamen, 24.48°N, 118.08°E; Shaowu, 27.33°N, 117.46°E; Fuzhou, 26.08°N,
209 119.28°E) are used to calculate trends in precipitable water vapor and CAPE. Daily
210 precipitable water and CAPE values are the mean of the two measurements made per
211 day.

212 **2.2.5 Satellite Datasets of Aerosol and Cloud Properties in Fujian Province,** 213 **China**

214 CloudSat data from 2006–2010 amassed over Fujian Province (22.5°N–28.5°N,
215 114.5°E–120.5°E) are used to extract cloud-top and cloud-base height information.
216 CloudSat retrievals of cloud-top and base heights are converted to temperatures using
217 temperature profiles from the European Center for Medium-range Weather
218 Forecasting Auxiliary product. The converted cloud-top and cloud-base temperatures
219 are used for cloud type classification. The classification of different cloud types is
220 summarized in Table 1 and introduced in sub-section 2.3.2. Only single-layer clouds
221 detected by the CloudSat are chosen here.

222 Aqua/MODIS retrievals of cloud droplet size and LWP for liquid clouds (clouds
223 with cloud-top temperatures (CTT) greater than 273 K) collected over Fujian
224 Province from 2003–2012 are used. **Errors in satellite retrievals of AOD such as**
225 **cloud contamination (Kaufman et al., 2005; Zhang et al., 2005) introduce**
226 **uncertainties in the aerosol-cloud relationship (Gryspeerd et al., 2014a, b). We use**
227 **MODIS Level 3 AOD with AOD > 0.6 excluded and not the higher resolution Level 2**

228 product to reduce the possibility of cloud contamination (Niu and Li, 2012) in AOD
229 retrievals.

230

231 **2.3 Methodology**

232

233 **2.3.1 Spatial and Temporal Matching of Model and Observation Data**

234 CPC-unified gauge-based daily precipitation data at a $0.5^\circ \times 0.5^\circ$
235 latitude-longitude resolution in the three countries for the year 2015 are used. GFS
236 model grid 004 data at the same latitude-longitude resolution ($0.5^\circ \times 0.5^\circ$) are also
237 used. Forecast precipitation for a one-day accumulation generated at three-hourly
238 intervals (e.g., at 03, 06, 09, 12, 15, 18, 21, 24 UTC), starting from the control time of
239 00 UTC, are used to match the corresponding gauge-based observations. The
240 MERRA-2 aerosol analysis is not coupled with GFS simulations. Daily MERRA-2
241 AOD is at a resolution of $0.625^\circ \times 0.5^\circ$ and is interpolated to the CPC and GFS
242 precipitation resolution using a linear interpolation method. The spatial and temporal
243 resolutions of the matched data sets are $0.5^\circ \times 0.5^\circ$ and are generated for each day.
244 There are ~3 686 000 grid points in total.

245 For the long-term analysis focused on Fujian, China, the NWP model reforecast
246 precipitation amount accumulated over the period of 12 hours to 36 hours out from
247 the 00 UTC run at six-hourly intervals and at a $1^\circ \times 1^\circ$ latitude-longitude resolution for
248 the years 1985 to 2010 are used to calculate the modeled daily precipitation amount in
249 each grid box. They are interpolated to match the long-term ground-based

250 precipitation observations recorded at each of the 67 stations in the study region of
251 Fujian, China (Fig. 1). There are 9495 days in total with matched data.

252 2.3.2 Rainfall Level Classification and Cloud Type Classification

253 Based on the definitions of the China Meteorological Administration,
254 precipitation data are classified into four groups according to the daily rain amount:
255 light rain (0.1–9.9 mm d⁻¹), moderate rain (10–24.9 mm d⁻¹), heavy rain (25–49.9 mm
256 d⁻¹), and very heavy rain (≥ 50 mm d⁻¹). Rain gauge data are usually used as reference
257 data in weather forecast and model evaluations because they come from direct
258 physical records (Tapiador et al., 2012). The most commonly-used rain detector is the
259 tipping bucket. Once the bucket is filled (0.1 mm), the bucket is emptied and produces
260 a signal. This process repeats until precipitation stops. Light rain less than 0.1 mm
261 cannot be measured. Therefore, the definition of light rain is 0.1–9.9 mm d⁻¹.

262 Table 1 summarizes the cloud types considered in the Fujian Province analysis.
263 Deep mixed-phase clouds are defined as clouds with cloud-base temperatures (CBT) >
264 15°C and CTT < -4°C, shallow mixed-phase clouds are defined as clouds with CBT
265 ranging from 0°C to 15°C and CTT < -4°C, and pure liquid clouds are defined as
266 clouds with CBT > 0°C and CTT > 0°C (Li et al., 2011; Niu & Li, 2012).

267 2.3.3 Evaluation Methods

268 Quantitative precipitation forecast scores developed by NCEP are used in the
269 evaluation. Table 2 is a contingency table based on documents from the World

270 Climate Research Programme

271 (http://www.cawcr.gov.au/projects/verification/#Methods_for_dichotomous_forecasts)

272). The most commonly-used statistical scores are the equitable threat score (ETS),
 273 which is also called the Gilbert skill score, and the bias score (BIAS). The ETS is
 274 given by

$$275 \quad ETS = \frac{H - H_{random}}{H + m + f - H_{random}}, \quad (2)$$

276 where H represents hits, f represents false alarms, and m represents misses. H_{random}
 277 is given by

$$278 \quad H_{random} = \frac{(H+m) \cdot (H+f)}{TOTAL}. \quad (3)$$

279 Its values range from -1/3 to 1 and a perfect score is 1. The BIAS is expressed as

$$280 \quad BIAS = \frac{H+f}{H+m}. \quad (4)$$

281 Its values range from 0 to infinity. A perfect score is 1. A BIAS < 1 indicates
 282 under-forecasting and a BIAS > 1 indicates over-forecasting.

283 Under limited ranges of LWP or RH, the top and bottom one-third of AOD
 284 values denote polluted and clean subsets of data. To obtain the forecast skill under a
 285 particular pollution condition, the ETS and the BIAS for clean and polluted conditions
 286 are calculated as

$$287 \quad \langle ETS \rangle_{i,j,m} = (ETS)_{i,j,m}, \quad (5)$$

$$288 \quad \langle BIAS \rangle_{i,j,m} = (BIAS)_{i,j,m}, \quad (6)$$

289 for the index of precipitation threshold (i), RH or LWP (j), and clean or polluted
 290 scenario (m).

291 **2.3.4 Statistical Method**

292 The standard deviation of the precipitation bias between the GFS model and CPC
 293 gauge data is calculated as

294
$$S = \sqrt{\frac{\sum(x-r)^2}{n-1}}, \quad (7)$$

295 where x is the forecast bias on a single day, n is equal to 364 days, and r is the mean
296 forecast bias. Pearson's method is used to calculate the linear correlation coefficient of
297 the relationship between the standard deviation of the forecast difference and AOD. A
298 t-test is applied with the p value set to 0.05.

299 The relative difference between the forecast precipitation and observations is
300 calculated as

301
$$\Delta P = \frac{P_{GFS/GEFS} - P_{OBV}}{P_{OBV}} \times 100\%, \quad (8)$$

302 where $P_{GFS/GEFS}$ refers to the forecast precipitation and P_{OBV} refers to the
303 precipitation from gauge-based observations.

304 For the long-term analysis, trends in a particular parameter are defined as the
305 relative change in the parameter (in %) over each successive decade (Lin & Zhao,
306 2009). The Mann-Kendall method is used to test the significance of the trend.

307

308 **3. Results**

309

310 **3.1 Evaluation of GFS Precipitation using the CPC Gauge-based Analysis**

311

312 **3.1.1 Annual Mean Patterns**

313 The CPC gauge-based precipitation analysis from 2015 is used to evaluate the
314 GFS precipitation forecast. Figure 2 shows the annual mean precipitation difference
315 between the GFS model and the CPC analysis for three countries, i.e., China, the U.S.,

316 and Australia, for the year 2015. Values above (below) zero represent the
317 overestimation (underestimation) of precipitation. In China (Figure 2a), the GFS
318 model overestimates the mean daily rainfall mostly in southwest China, especially in
319 Sichuan, Yunnan, and Guizhou Provinces (by $\sim 3 \text{ mm d}^{-1}$), and in northwest China
320 where rain events are scarcer. Rainfall is underestimated over the Yangtze River Delta
321 region and the eastern coast of China. In the U.S. (Figure 2b), the GFS model
322 overestimates precipitation by about $1\text{--}2 \text{ mm d}^{-1}$ in most regions and underestimates
323 precipitation along the coastline of the Gulf of Mexico (by $\sim 1 \text{ mm d}^{-1}$). In Australia
324 (Figure 2c), the forecast performance is good. In northern Australia, the
325 underestimation of precipitation is around 2 mm d^{-1} . Z-scores were calculated to test
326 the significance of the annual mean difference in the daily rainfall amount between
327 the GFS model forecast and the CPC analysis. Z values range from -0.4803 to 0.8534
328 over the grids in the three countries. Because the Z-score values are less than 2, this
329 indicates that the mean difference is not significant at the two-sigma level. Therefore,
330 the forecast performance of the GFS model with regard to the annual mean daily
331 rainfall in the three countries is sound with reference to the gauge-based CPC rainfall
332 analysis.

333 **3.1.2 Different Rainfall Intensities**

334 Figure 3 shows the annual mean relative difference between forecast
335 precipitation and observations for light rain ($0.1\text{--}10 \text{ mm d}^{-1}$) and heavier rain (> 10
336 mm d^{-1}). The GFS model overestimates light rain in most places (Figure 3a) and
337 underestimates heavier rain (Figure 3b). This suggests that both the overestimation of

338 light rain and underestimation of moderate rain, heavy rain, and very heavy rain
339 contribute to the forecast bias. Figure 4 shows the mean relative difference between
340 forecast and observed daily precipitation amounts for different rain intensities in the
341 three countries for the whole year (Fig. 4a) and for summer only (Fig. 4b). GFS
342 forecasts overestimate light rain by 47.84% and underestimate moderate rain, heavy
343 rain, and very heavy rain by 31.83%, 52.94%, and 65.74%, respectively (Fig. 4a). The
344 underestimation of precipitation in summer is larger for moderate rain (32.93%),
345 heavy rain (55.19%), and very heavy rain (66.93%, Fig. 4b). These model biases are
346 caused by many factors that are beyond the scope of this paper to examine. Our focus
347 is on any potential contribution of neglecting aerosol effects to the biases. The
348 relationship between model performance and AOD is thus further investigated.

349 **3.1.3 Relationship between Model Performance and AOD**

350 In principle, the underestimation and overestimation at different rainfall levels
351 (Figs. 3 and 4) may be linked to AOD conditions, as elaborated in the introduction of
352 previous studies (c.f. the review of Tao et al., 2012). The standard deviation of the
353 forecast bias at each grid point in the three countries is calculated to further examine
354 the links between the model bias and AOD. Aerosols tend to polarize precipitation by
355 suppressing light rain and enhancing heavy rain, and thus increase the standard
356 deviation. The calculation of the standard deviation of the forecast difference is based
357 on Eqn. (7). Figure 5 shows the relationship between the standard deviation and AOD
358 in the three countries. Each point represents a grid box. The standard deviation and
359 AOD has a significant positive correlation in the three countries with correlation

360 coefficients of 0.5602, 0.6522, and 0.5182 for Australia, the U.S., and China,
361 respectively. This suggests that the degree of disparity of the forecast error is larger
362 for grids with high aerosol loading. The slopes of the best-fit lines are 75.23 for
363 relatively clean Australia (maximum AOD < 0.18), 48.4 for the polluted U.S.
364 (maximum AOD < 0.20), and 8.554 for heavily polluted China (maximum AOD >
365 0.60).

366 The ETS and BIAS are used to examine the model performance under clean and
367 polluted conditions for different AOD bins with fixed LWP (Figs. 6a and 6c) or RH
368 (Figs. 6b and 6d) in the three countries. For a particular LWP or RH condition, the top
369 and bottom one-third of AOD values are defined as polluted and clean subsets of data.
370 In Figs. 6a and 6b, ETS increases as the LWP or RH increases. This is because
371 large-scale precipitation is diagnosed from cloud mixing ratios. The ETS are smaller
372 for the polluted scenario than for the clean scenario, especially under high LWP or
373 high RH conditions. In Figs. 6c and 6d, the BIAS decreases under polluted conditions
374 compared with the BIAS under clean conditions. The decreases in ETS and BIAS
375 under polluted conditions suggest that AOD influences the model rainfall forecast.

376

377 **3.2 Potential Contribution of Aerosols to the Model Bias**

378

379 **3.2.1 Long-term Forecast Bias and Trends in Observed Precipitation in Fujian** 380 **Province, China**

381 The model performance differs under different conditions, e.g., initial and

382 dynamic settings, and weather regimes. A long-term statistical evaluation of rainfall
383 forecasts for Fujian Province is made to mitigate these fluctuations in the model
384 forecast accuracy. Model data from 1985 to 2010 are used to calculate the relative
385 difference based on Eqn. (8). Figure 7 shows the mean relative difference between
386 forecast and observed precipitation for different rain rates from the 67 stations in
387 Fujian Province for all seasons and for summer only. Figure 7a shows that there is
388 114.36% more precipitation forecast by the NCEP/GEFS model than observed for the
389 light rain cases. For moderate rain, heavy rain, and very heavy rain cases, 29.20%,
390 41.74%, and 59.30% less precipitation than observed, respectively, was forecast. The
391 underestimation of moderate rain (46.88%), heavy rain (59.58%), and very heavy rain
392 (70.16%) is even larger in summer (Fig. 7b).

393 Seasonally-averaged trends (percent change per decade) in daily rain amount and
394 frequency over Fujian Province from 1980 to 2009 are calculated. Only the results for
395 rain amount are shown in Fig. 8 because the frequency results bear a close
396 resemblance. Cross-hatched bars represent data at a confidence level greater than 95%.
397 In spring, daily rain amounts decreased over time, ranging from -4.9% to -15.3% per
398 decade for different rain rates. In summer, heavy and very heavy daily rain amounts
399 increased significantly. For very heavy rain, the amount and frequencies increased at a
400 rate of 21.8% and 24.5% (not shown), respectively. In autumn, light rain and
401 moderate rain amounts decreased. In winter, the light rain amount decreased over time.
402 Decreases in light rain amounts are -8.4% per decade. Overall, the increasing trends in
403 summertime for heavy and very heavy rain are most significant. The decreasing

404 trends in light rain in other seasons are also significant.

405 **3.2.2 Examination of Potential Contributors**

406 Reasons for the difference between modeled and observed precipitation are
407 examined in terms of aerosol effects, water vapor, and CAPE. Time series of visibility
408 over the period of 1980–2009 are shown in Fig. 9. Visibility has declined steadily in
409 all seasons but summer during which there was a short-lived increasing trend from
410 1992–1997. The linear declining trends are statistically significant at the 95%
411 confidence level. The greatest reduction is seen during the summer, especially after
412 1997. Tables 3 and 4 summarize the correlation between visibility and precipitation
413 amount and frequency, respectively. A positive (negative) correlation between
414 visibility and precipitation means a negative (positive) correlation between aerosol
415 concentration and precipitation. Values with an asterisk represent data at a confidence
416 level greater than 95%. For light rain, the correlations between daily rain amount and
417 visibility (Table 3) and between rain frequency and visibility (Table 4) are positive for
418 all seasons. For heavy rain to very heavy rain, the correlations between visibility and
419 daily rain amount (Table 3), as well as frequency (Table 4), are negative in summer.

420 The water vapor amount and atmospheric stability are important factors related
421 to precipitation. To analyze the potential contributions of these factors to the forecast
422 bias, their effects on precipitation are examined. Data from three atmospheric
423 sounding stations (Xiamen, 24.48°N, 118.08°E; Shaowu, 27.33°N, 117.46°E; Fuzhou,
424 26.08°N, 119.28°E) collected from 1980–2009 are used to calculate trends in
425 precipitable water vapor and CAPE. Figure 10 shows time series of annual mean

426 water vapor amount for different seasons. A slight increasing trend is seen in winter,
427 while no discernible trend is seen in other seasons. This suggests that the water vapor
428 amount characterizing the study region cannot explain seasonal variations in
429 precipitation. Time series of mean CAPE for the different seasons are shown in Fig.
430 11. There is an increasing trend in summertime CAPE during the period of 1980–2009,
431 but the trends are not as strong in other seasons. The observed increase in rain amount
432 in summer is in part likely due to an increase in convective precipitation events that
433 arises from the increasing trend in CAPE.

434 **3.2.3 Impact of Aerosols on Clouds and Precipitation**

435 Aerosols can influence precipitation through warm- and cold-rain processes (Tao
436 et al., 2012). Cloud droplet size, LWP for clouds with CTT greater than 273 K, and
437 AOD at 550 nm retrieved from the Aqua/MODIS platform over Fujian Province
438 during the period of 2003–2012 are used to examine the impact of aerosols on cloud
439 effective radius (CER). Figure 12 shows CER as a function of AOD for liquid clouds
440 with different LWPs. When the AOD is small (< 0.2), the CER increases with
441 increasing LWP. For $LWP > 100 \text{ g m}^{-2}$, the CER decreases with increasing AOD,
442 which suggests that more aerosols decrease CERs. This result is in line with the two
443 aerosol indirect effects (Twomey et al., 1984; Albrecht, 1989). A greater number of
444 smaller droplets may reduce the precipitation efficiency and suppress or enhance
445 precipitation, as reviewed by Tao et al. (2012).

446 Several observational and model studies suggest that smaller cloud particles are
447 more likely to ascend to above the freezing level, releasing latent heat and

448 invigorating deep convection (Rosenfeld et al., 2008; Li et al., 2011) while
449 suppressing shallow convection. CTTs and CBTs, converted from CloudSat
450 measurements of cloud top and base heights, in Fujian Province from 2006 to 2010
451 are used to study the impact of aerosols on the cloud development of different clouds.
452 Figure 13 shows CTT as a function of AOD for liquid and warm- and cold-base
453 mixed-phase clouds. Definitions of the different cloud types are summarized in Table
454 1, which is taken from Li et al. (2011). Left-hand ordinates are for liquid clouds, while
455 right-hand ordinates are for warm-base and cold-base mixed-phase clouds. For all
456 seasons (Fig. 13a), CTTs of warm-base mixed-phase clouds are lower than those of
457 cold-base mixed-phase clouds. Warm-base mixed-phase CTTs decrease with
458 increasing AOD, which indicates that cloud-top heights have increased. For cold-base
459 mixed-phase clouds, variations in CTT with AOD are not obvious. For liquid clouds,
460 CTTs increase slightly with AOD, which means that the development of liquid clouds
461 is suppressed when AOD increases. The negative slope of the linear relationship
462 between CTT and AOD for warm-base mixed-phase clouds and the positive slope of
463 the linear relationship between CTT and AOD for liquid clouds are both stronger in
464 summer (Fig. 13b). This suggests that aerosols inhibit the development of shallow
465 liquid clouds and invigorate warm-base mixed-phase clouds, with little influence on
466 cold-base mixed-phase clouds. These effects of aerosols on summertime cloud
467 development are more obvious, likely because convective clouds occur more
468 frequently during the summertime in Fujian Province.

469 These results agree with those from a ground-based study using ARM Southern

470 Great Plains data (Li et al., 2011) and from tropical region studies using
471 CloudSat/Cloud-Aerosol Lidar and Infrared Pathfinder Satellite Observation data (Niu
472 & Li, 2012; Peng et al., 2016). The impact of aerosols on different types of clouds
473 may lead to light rain suppression and heavier rain enhancement. If the GFS model
474 neglects aerosol effects, overestimations of light rain and underestimations of heavy
475 to very heavy rain may be forecast, especially in summer. For example, Fig. 14 shows
476 time series of regionally-averaged daily modeled and observed precipitation in 2001.
477 Modeled and observed precipitation amounts over the region agree well in spring and
478 winter while modeled precipitation amounts are greater than observations for light
479 rain in autumn. Note that modeled precipitation amounts are significantly less than
480 observed precipitation amounts over the region in summer when deep convective
481 clouds and heavy to very heavy rain tends to occur. Although there are many reasons
482 for the difference between modeled and observed precipitation, these results suggest
483 that to some extent, the neglect of aerosol effects may contribute to the model rainfall
484 forecast bias.

485

486 **4. Summary and Discussion**

487

488 Aerosol-cloud interactions (ACI) have been recognized as playing a vital role in
489 precipitation, but have not been considered in the National Centers for Environmental
490 Prediction (NCEP) Global Forecast System (GFS) model yet. For more efficient and
491 accurate forecasts, new physical schemes are being incorporated into the NCEP's

492 Next-Generation Global Prediction System. As a benchmark evaluation of model
493 results that exclude aerosol effects, the operational precipitation forecast (before any
494 ACI are included) is evaluated using multiple datasets with the goal of determining if
495 there is any link between the model forecast bias and aerosol loading. Multiple
496 datasets are used, including ground-based precipitation and visibility datasets,
497 Aqua/Moderate Resolution Imaging Spectroradiometer products, CloudSat retrievals
498 of cloud-base and cloud-top heights, Modern-Era Retrospective analysis for Research
499 and Applications Version 2 model simulations of aerosol optical depth (AOD), and
500 GFS forecast datasets.

501 Operational daily precipitation forecasts for the year 2015 in three countries, i.e.,
502 Australia, the U.S., and China, were evaluated. The model overestimates light rain,
503 and underestimates moderate rain, heavy rain, and very heavy rain. The
504 underestimation of precipitation in summer is even larger. This is consistent
505 qualitatively with expected results because the model does not account for aerosol
506 effects on precipitation, i.e., the inhibition of light rain and enhancement of heavy rain
507 by aerosols. The standard deviations of forecast differences are generally positively
508 correlated with increasing aerosol loadings in the three countries. **Equitable threat**
509 **scores and BIAS scores decrease for the polluted scenario.**

510 An analysis of long-term measurements from Fujian Province, China was done.
511 Light rain overestimation, and moderate, heavy, and very heavy rain underestimations
512 from the Global Ensemble Forecast System were also seen. The underestimation for
513 stronger rainfall was larger in the summertime. Increasing trends for heavy and very

514 heavy rain in summer, and decreasing trends for light rainfall in other seasons were
515 significant from 1980 to 2009. Long-term analyses show that neither water vapor nor
516 convective available potential energy can explain these trends. Satellite datasets
517 amassed in Fujian Province from 2006 to 2010 were used to shed more light on the
518 impact of aerosols on cloud and precipitation. As implied by the Twomey effect, cloud
519 effective radii decrease with increasing AOD, which likely suppresses light rain and
520 enhances heavy rain. This may contribute to the model forecast bias to some extent.
521 The underestimation of heavy rain in summer most likely occurs because deep
522 convective clouds occur more frequently during the summertime in Fujian Province.
523 How neglecting ACI in the operational forecast model impacts model biases remains
524 an open question. This study is arguably the first attempt at evaluating numerical
525 weather prediction forecast errors in terms of the potential effects of aerosols. A more
526 rigorous and systematic evaluation to gain insights into the model is needed. Toward
527 this goal, case-based investigations using rich instantaneous measurements are
528 currently underway.

529 **Data Availability**

530 Forecast data are from the NOAA NOMADS (<https://nomads.ncdc.noaa.gov/>)
531 for GFS data (<https://nomads.ncdc.noaa.gov/data/gfs4/>) and the NOAA NCDC
532 ([https://www.ncdc.noaa.gov/data-access/model-data/model-datasets/global-ensemble-
533 forecast-system-gefs](https://www.ncdc.noaa.gov/data-access/model-data/model-datasets/global-ensemble-forecast-system-gefs)) for GEFS reforecast data. NASA MERRA-2 aerosol data are
534 accessible from the NASA Global Modeling and Assimilation Office
535 (https://gmao.gsfc.nasa.gov/reanalysis/MERRA-2/data_access/). The CPC Unified
536 Gauge-Based Analysis of Global Daily Precipitation dataset is available at
537 [https://climatedataguide.ucar.edu/climate-data/cpc-unified-gauge-based-analysis-glob
538 al-daily-precipitation](https://climatedataguide.ucar.edu/climate-data/cpc-unified-gauge-based-analysis-global-daily-precipitation). ECMWF reanalysis data are accessible via
539 <http://apps.ecmwf.int/datasets/data/interim-full-daily/>. MODIS data and CloudSat data
540 are available at <https://modis.gsfc.nasa.gov/data/> and
541 <http://www.cloudsat.cira.colostate.edu/>, respectively. Ground-based observations of
542 precipitation amount, visibility, precipitable water, and CAPE from Fujian Province
543 can be requested from the Chinese Meteorological Administration's National
544 Meteorological Information Center (<http://cdc.cmic.cn> and <http://data.cma.cn/>).

545 **Acknowledgements**

546 This study was supported by the Ministry of Science and Technology of China
547 (2013CB955804), the Fundamental Research Funds for the Central Universities of
548 China (312231103), State Key Laboratory of Earth Surface Processes and Resource
549 Ecology (2015-TDZD-090), and NOAA (NA15NWS4680011). We would like to
550 thank the NASA Global Modeling and Assimilation Office
551 (https://gmao.gsfc.nasa.gov/reanalysis/MERRA-2/data_access/) and the Goddard
552 Space Flight Center Distributed Active Archive Center for their help in accessing
553 MERRA-2 inst3_2d_gas_Nx: 2d, 3-Hourly, Instantaneous, Single-Level, Assimilation,
554 Aerosol Optical Depth Analysis Version 5.12.4 data. We would also like to thank the
555 staff at the National Center for Atmospheric Research responsible for creating the
556 "The Climate Data Guide: CPC Unified Gauge-Based Analysis of Global Daily
557 Precipitation"
558 (<https://climatedataguide.ucar.edu/climate-data/cpc-unified-gauge-based-analysis-glob>
559 [al-daily-precipitation](https://climatedataguide.ucar.edu/climate-data/cpc-unified-gauge-based-analysis-glob)). Thanks also go to the NOAA NOMADS
560 (<https://nomads.ncdc.noaa.gov/>) for GFS data
561 (<https://nomads.ncdc.noaa.gov/data/gfs4/>), the NOAA NCDC
562 ([https://www.ncdc.noaa.gov/data-access/model-data/model-datasets/global-ensemble-](https://www.ncdc.noaa.gov/data-access/model-data/model-datasets/global-ensemble-forecast-system-gefs)
563 [forecast-system-gefs](https://www.ncdc.noaa.gov/data-access/model-data/model-datasets/global-ensemble-forecast-system-gefs)) for GEFS reforecast data, and the NWS CPC for data
564 downloading software (http://www.cpc.ncep.noaa.gov/products/wesley/get_gfs.html).
565 We acknowledge the Chinese Meteorological Administration's National
566 Meteorological Information Center (<http://cdc.cmic.cn> and <http://data.cma.cn/>), the
567 European Centre for Medium-Range Weather Forecasts (ECMWF)
568 (<http://www.ecmwf.int/>), the NASA Goddard Space Flight Center
569 (<https://modis.gsfc.nasa.gov/data/>), and the CloudSat Data Processing Center

570 (<http://www.cloudsat.cira.colostate.edu/>) for providing the various datasets used in the
571 study.

572 We would also like to thank Drs. Shrinivas Moorthi, and Jun Wang from NOAA,
573 Sarah Lu from State University of New York, Albany, Dr. Seoung-Soo Lee from the
574 University of Maryland, and Drs. Duoying Ji and Lanning Wang from Beijing Normal
575 University for their discussions regarding this study. We especially appreciate the help
576 given by Dr. Jongil Han in understanding the GFS/GEFS models and data products,
577 and the guidance provided by Dr. Hye-Lim Yoo. We also greatly appreciate the
578 valuable comments from the anonymous reviewers.

579

580

581 **References**

582

583 Ackerman, A. S., Toon, O. B. , Stevens, D. E., Heymsfield, A. J., Ramanathan, V., and Welton, E.
584 J.: Reduction of tropical cloudiness by soot, *Science*, 288(5468), 1042–1047,
585 doi:10.1126/science.288.5468.1042, 2000.

586 Albrecht, B. A.: Aerosols, cloud microphysics, and fractional cloudiness, *Science*, 245(4923),
587 1227–1230, doi:10.1126/science.245.4923.1227, 1989.

588 Andreae, M. O., Rosenfeld, D., Artaxo, P., Costa, A. A., Frank, G. P., Longo, K. M., and
589 Silva-Dias, M. A. F.: Smoking rain clouds over the Amazon, *Science*, 303(5662), 1337–1342,
590 doi:10.1126/science.1092779, 2004.

591 Appel, B. R., Tokiwa, Y., Hsu, J., Kothny, E. L., and Hahn, E.: Visibility as related to atmospheric
592 aerosol constituents, *Atmos. Environ.*, 19, 1525–1534, doi: 10.1016/j.bbr.2011.03.031, 1985.

593 Arakawa, A., and Schubert, W. H.: Interaction of a cumulus cloud ensemble with the large-scale
594 environment. Part I. *J. Atmos. Sci.*, 31, 674–701,
595 doi:10.1175/1520-0469(1974)031<0674:IOACCE>2.0.CO;2, 1974.

596 Bell, T., Rosenfeld, D., Kim, K., Yoo, J., Lee, M., and Hahnenberger, M.: Midweek increase in
597 U.S. summer rain and storm heights suggests air pollution invigorates rainstorms, *J. Geophys.*
598 *Res. Atmos.*, 113, D02209, doi:10.1029/2007JD008623, 2008.

599 Carrió G. G., Cotton, W. R., and Cheng, W. Y. Y.: Urban growth and aerosol effects on
600 convection over Houston. Part I: The August 2000 case, *Atmos. Res.*, 96(4), 560–574, doi:
601 10.1016/j.atmosres.2010.01.005, 2010.

602 Charlson, R. J.: Atmospheric visibility related to aerosol mass concentration: Review, *Environ. Sci.*
603 *Technol.*, 3, 913–918, doi:10.1021/es60033a002, 1969.

604 Chin, M., Ginoux, P., Kinne, S., Torres, O., Holben, B., Duncan, B. N., Martin, R. V., Logan, J.,
605 Higurashi, A., and Nakajima, T.: Tropospheric aerosol optical thickness from the GOCART
606 model and comparisons with satellite and Sun photometer measurements, *J. Atmos. Phys.*, 59,
607 461–483, doi:10.1175/1520-0469(2002)059<0461:TAOTFT>2.0.CO;2, 2002.

608 da Silva, A., Colarco, P. R., Darmenoy, A. S., Buchard-Marchant, V., Randles, C. A., and Gupta, P.:
609 An overview of the GEOS-5 Aerosol Reanalysis, American Geophysical Union, Fall Meeting

610 2011, abstract #A52D-09, San Francisco, CA, USA, 2011.

611 Fan, J. W., Rosenfeld, D., Yang, Y., Zhao, C., Leung, L. R., and Li, Z.: Substantial contribution of
612 anthropogenic air pollution to catastrophic floods in Southwest China, *Geophys. Res. Lett.*,
613 42(14), 6066–6075, doi:10.1002/2015GL064479, 2015.

614 Fan, J. W., Wang, Y., Rosenfeld, D., and Liu, X.: Review of aerosol–cloud interactions:
615 mechanisms, significance, and challenges, *J. Atmos. Sci.*, 73(11), 4221–4252,
616 doi:10.1175/JAS-D-16-0037.1, 2016.

617 GCWM Branch, EMC: The GFS atmospheric model. NCEP Office Note 442, 14 pp., available at:
618 <http://wwwt.emc.ncep.noaa.gov/officenotes>, 2003.

619 Grell, G. A.: Prognostic evaluation of assumptions used by cumulus parameterizations, *Mon. Wea.*
620 *Rev.*, 121, 764–787, doi:10.1175/1520-0493(1993)121<0764:PEOAUB>2.0.CO;2, 1993.

621 Gryspeerdt, E., Stier, P. and Partridge, D.G.: Satellite observations of cloud regime development:
622 The role of aerosol processes, *Atmos. Chem. Phys.*, 14(3), 1141–1158,
623 doi:10.5194/acp-14-1141-2014, 2014a.

624 Gryspeerdt, E., Stier, P. and Partridge, D.G.: Links between satellite-retrieved aerosol and
625 precipitation, *Atmos. Chem. Phys.*, 14(18), 9677–9694, doi:10.5194/acp-14-9677-2014,
626 2014b.

627 Han, J., and Pan, H. L.: Revision of convection and vertical diffusion schemes in the NCEP Global
628 Forecast System, *Wea. Forecasting*, 26, 520–533, doi:10.1175/WAF-D-10-05038.1, 2011.

629 Han, J., Witek, M. L., Teixeira, J., Sun, R., Pan, H. L., Fletcher, J. K., and Bretherton, C. S.:
630 Implementation in the NCEP GFS of a Hybrid Eddy-Diffusivity Mass-Flux (EDMF)
631 boundary layer parameterization with dissipative heating and modified stable boundary layer
632 mixing, *Wea. Forecasting*, 31(1), 341–352, doi:10.1175/WAF-D-15-0053.1, 2016.

633 Hong, S. Y., and Pan, H. L.: Nonlocal boundary layer vertical diffusion in a medium-range
634 forecast model, *Mon. Wea. Rev.*, 124, 2322–2339,
635 doi:10.1175/1520-0493(1996)124<2322:NBLVDI>2.0.CO;2, 1996.

636 Intergovernmental Panel on Climate Change: Climate Change 2013: The Physical Science Basis,
637 in Contribution of Working Group I to the Fifth Assessment Report of the Intergovernmental
638 Panel on Climate Change, Cambridge Univ. Press, Cambridge, U. K., 2013.

639 Jiang, H., Xue, H., Teller, A., Feingold, G., and Levin, Z.: Aerosol effects on the lifetime of
640 shallow cumulus, *Geophys. Res. Lett.*, 33(14), doi:10.1029/2006gl026024, 2006.

641 Jiang, M., Li, Z., Wan, B., and Cribb, M.: Impact of aerosols on precipitation from deep
642 convective clouds in eastern China, *J. Geophys. Res. Atmos.*, 121(16), 9607–9620,
643 doi:10.1002/2015JD024246, 2016.

644 Kanamitsu, M.: Description of the NMC Global Data Assimilation and Forecast System, *Wea.*
645 *Forecasting*, 4(3), 335–342, doi:10.1175/1520-0434(1989)004<0335:DOTNGD>2.0.CO;2,
646 1989.

647 Kaufman, Y., Koren, I., Remer, L., Rosenfeld, D., and Rudich, Y.: The effect of smoke, dust, and
648 pollution aerosol on shallow cloud development over the Atlantic Ocean, *Proc. Nat. Acad.*
649 *Sci. USA*, 102(32), 11,207–11,212, doi:10.1073/pnas.0505191102, 2005.

650 Khain, A., Benmoshe, N., and Pokrovsky, A.: Factors determining the impact of aerosols on
651 surface precipitation from clouds: An attempt at classification, *J. Atmos. Sci.*, 65(5), 1721–
652 1748, doi:10.1175/2007JAS2515.1, 2008.

653 Koren, I., Kaufman, Y. J., Rosenfeld, D., Remer, L. A., and Rudich, Y.: Aerosol invigoration and
654 restructuring of Atlantic convective clouds, *Geophys. Res. Lett.*, 32(14), doi:
655 10.1029/2005gl023187, 2005.

656 Koren, I., Martins, J. V., Remer, L. A., and Afargan, H.: Smoke invigoration versus inhibition of
657 clouds over the Amazon, *Science*, 321(5891), 946–949, doi:10.1126/science.1159185, 2008.

658 Li, Z., Niu, F., Fan, J., Liu, Y., Rosenfeld, D., and Ding, Y.: Long-term impacts of aerosols on the
659 vertical development of clouds and precipitation, *Nat. Geosci.*, 4(12), 888–894,
660 doi:10.1038/ngeo1313, 2011.

661 Li, Z., Lau, W. K.-M., Ramanathan, V., Wu, G., Ding, Y., Manoj, M. G., Liu, J., Qian, Y., Li, J.,
662 Zhou, T., Fan, J., Rosenfeld, D., Ming, Y., Wang, Y., Huang, J., Wang, B., Xu, X., Lee, S.-S.,
663 Cribb, M., Zhang, F., Yang, X., Zhao, C., Takemura, T., Wang, K., Xia, X., Yin, Y., Zhang, H.,
664 Guo, J., Zhai, P. M., Sugimoto, N., Babu, S. S., and Brasseur, G. P.: Aerosol and monsoon
665 climate interactions over Asia, *Rev. Geophys.*, 54(4), 866–929, doi:10.1002/2015RG000500,
666 2016.

667 Lin, Y., and Zhao, C.: Trends of precipitation of different intensity in China, *Acta Scientiarum*

668 Naturalium Universitatis Pekinensis, 45, 995–1002, 2009.

669 Lin, J. C., Matsui, T., Pielke, R. A., and Kummerow, C.: Effects of biomass-burning-derived
670 aerosols on precipitation and clouds in the Amazon Basin: a satellite-based empirical study, J.
671 Geophys. Res. Atmos., 111(D19), doi:10.1029/2005jd006884, 2006.

672 Moorthi, S., Pan, H. L., and Caplan, P.: Changes to the 2001 NCEP operational MRF/AVN global
673 analysis/forecast system, NWS Technical Procedures Bulletin, 484, available online at www.
674 nws.noaa.gov/om/tpb/484.htm, 2001.

675 Niu, F., and Li, Z.: Systematic variations of cloud top temperature and precipitation rate with
676 aerosols over the global tropics, Atmos. Chem. Phys., 12(18), 8491–8498,
677 doi:10.5194/acp-12-8491-2012, 2012.

678 Pan, H. L., and Wu, W. S.: Implementing a mass flux convective parameterization package for the
679 NMC Medium-Range Forecast model, NMC Office Note 409, 40 pp, 1995.

680 Peng, J., Li, Z., Zhang, H., Liu, J., and Cribb, M. C.: Systematic changes in cloud radiative forcing
681 with aerosol loading for deep clouds in the tropics, J. Atmos. Sci., 73, 231–249,
682 doi:10.1175/JAS-D-15-0080.1, 2016.

683 Randles, C. A., da Silva, A. M., Buchard, V., Darmenoy, A., Colarco, P. R., Aquila, V., Bian, H.,
684 Nowotnick, E. P., Pan, X., Smirnov, A., Yu, H., and Govindaraju, R.: The MERRA-2
685 Aerosol Assimilation, NASA Tech. Rep. Series on Global Modeling and Data Assimilation,
686 NASA TM—2016-104606, 45, 156 pp, 2016.

687 Rienecker, M. M., Suarez, M. J., Gelaro, R., Todling, R., Bacmeister, J., Liu, E., Bosilovich, M. G.,
688 Schubert, S. D., Takacs, L., Kim, G. K., Bloom, S., Chen, J., Collins, D., Conaty, A., da Silva,
689 A., Gu, W., Joiner, J., Koster, R. D., Lucchesi, R., Molod, A., Owens, T., Pawson, S., Pegion,
690 P., Redder, C. R., Reichle, R., Robertson, F. R., Ruddick, A. G., Sienkiewicz, M., and
691 Woollen, J.: MERRA: NASA's Modern-Era Retrospective Analysis for Research and
692 Applications, J. Climate, 24(14), 3624–3648, doi:10.1175/JCLI-D-11-00015.1, 2011.

693 Rosenfeld, D.: Suppression of rain and snow by urban and industrial air pollution, Science,
694 287(5459), 1793–1796, doi:10.1126/science.287.5459.1793, 2000.

695 Rosenfeld, D., Dai, J., Yu, X., Yao, Z., Xu, X., Yang, X., and Du, C.: Inverse relations between
696 amounts of air pollution and orographic precipitation, Science, 315, 1396–1398,

697 doi:10.1126/science.1137949, 2007.

698 Rosenfeld, D., Lohmann, U., Raga, G.B., Dowd, C. D. O., Kulmala, M., Fuzzi, S., Reissell, A.,
699 and Andreae, M. O.: Flood or drought: How do aerosols affect precipitation?, *Science*,
700 321(5894), 1309–1313, doi:10.1126/science.1160606, 2008.

701 Sela, J.: Implementation of the sigma pressure hybrid coordinate into GFS; NCEP Office, Note #
702 461, available at <http://www.emc.ncep.noaa.gov/officenotes/FullTOC.html#2000>, 2009.

703 Sundqvist, H., Berge, E., and Kristjansson, J. E.: Condensation and cloud parameterization studies
704 with a mesoscale numerical weather prediction model, *Mon. Wea. Rev.*, 117, 1641–1657,
705 doi:10.1175/1520-0493(1989)117<1641:CACPSW>2.0.CO%3B2, 1989.

706 Tao, W. K., Chen, J. P., Li, Z., Wang, C., and Zhang, C.: Impact of aerosols on convective clouds
707 and precipitation, *Rev. Geophys.*, 50(2), doi:10.1029/2011rg000369, 2012.

708 Tapiador, F. J., Turk, F. J., Petersen, W., Hou, A. Y., Garc á-Ortega, E., Machado, L. A., Angelis, C.
709 F., Salio, P., Kidd, C., Huffman, G. J., and De Castro, M.: Global precipitation measurement:
710 Methods, datasets and applications, *Atmos. Res.*, 104, 70–97,
711 <https://doi.org/10.1016/j.atmosres.2011.10.021>, 2012.

712 Troen, I., and Mahrt, L.: A simple model of the atmospheric boundary layer: Sensitivity to surface
713 evaporation, *Bound.-Layer Meteor.*, 37, 129–148, doi: 10.1007/BF00122760, 1986.

714 Twomey, S. A., Pieprgrass, M., and Wolfe, T. L.: An assessment of the impact of pollution on
715 global cloud albedo, *Tellus B*, 36(5), 356–366, doi:10.1111/j.1600-0889.1984.tb00254.x,
716 1984.

717 van den Heever, S. C., Stephens, G. L., and Wood, N. B.: Aerosol indirect effects on tropical
718 convection characteristics under conditions of radiative–convective equilibrium, *J. Atmos.*
719 *Sci.*, 68(4), 699–718, doi: <http://dx.doi.org/10.1175/2010JAS3603.1>, 2011.

720 Xie, P. P., Yatagai, A., Chen, M. Y., Hayasaka, T., Fukushima, Y., Liu, C. M., and Yang, S.: A
721 gauge-based analysis of daily precipitation over East Asia, *J. Hydrometeorol.*, 8(3), 607–626,
722 doi:10.1175/Jhm583.1, 2007.

723 Xue, H., and Feingold, G.: Large-eddy simulations of trade wind cumuli: investigation of aerosol
724 indirect effects, *J. Atmos. Sci.*, 63(6), 1605–1622, doi:10.1175/JAS3706.1, 2006.

725 Yang, F. L., Pan., H. L., Krueger, S. K., Moorthi, S., and Lord, S. J.: Evaluation of the NCEP

726 Global Forecast System at the ARM SGP site, *Mon. Wea. Rev.*, 134(12), 3668–3690,
727 doi:10.1175/MWR3264.1, 2006.

728 Yang, X., and Li, Z.: Increases in thunderstorm activity and relationships with air pollution in
729 southeast China, *J. Geophys. Res. Atmos.*, 119, 1835–1844, doi:10.1002/2013JD021224,
730 2014.

731 Yang, X., Ferrat, M., and Li, Z.: New evidence of orographic precipitation suppression by aerosols
732 in central China, *Meteor. Atmos. Phys.*, 119, 17–29, doi:10.1007/s00703-012-0221-9, 2013.

733 Yoo, H., and Li, Z.: Evaluation of cloud properties in the NOAA/NCEP global forecast system
734 using multiple satellite products, *Clim. Dyn.*, 39, 2769–2787,
735 doi:10.1007/s00382-012-1430-0, 2012.

736 Yoo, H., Li, Z., Hou, Y.-T., Lord, S., Weng, F., and Barker, H. W.: Diagnosis and testing of
737 low-level cloud parameterizations for the NCEP/GFS model satellite and ground-based
738 measurements, *Clim. Dyn.*, 41, 1595–1613, doi:10.1007/s00382-013-1884-8, 2013.

739 Zhang, J., Reid, J., and Holben, B.: An analysis of potential cloud artifacts in MODIS over ocean
740 aerosol optical thickness products, *Geophys. Res. Lett.*, 32, L15803,
741 doi:10.1029/2005GL023254, 2005.

742 Zhao, Q. Y., and Carr, F. H.: A prognostic cloud scheme for operational NWP models, *Mon. Wea.*
743 *Rev.*, 125, 1931–1953, doi:10.1175/1520-0493(1997)125<1931:APCSFO>2.0.CO;2, 1997.

744

745 **Table 1.** Definitions of warm- and cold-base mixed-phase clouds and liquid clouds.

	Cloud-base temperature (°C)	Cloud-top temperature (°C)
Deep mixed-phase clouds with warm bases	> 15	< -4
Shallow mixed-phase clouds with cold bases	0–15	< -4
Liquid clouds	> 0	> 0

746

747

748 **Table 2.** Contingency table.

Observed	Observed yes	Observed no
Forecast		
Forecast yes	Hits	False alarms
Forecast no	Misses	Correct negatives

749

750

751 **Table 3.** Correlation coefficients from linear regressions of visibility and different rain
752 amount types for all seasons.

Rain rate	Light rain	Moderate rain	Heavy rain	Very heavy rain	Rain amount
Spring	0.48*	0.51*	0.48*	0.17	0.40*
Summer	0.08	-0.16	-0.28	-0.41*	-0.38*
Autumn	0.31	0.18	0.26	-0.22	0.11
Winter	0.55*	0.26	0.26	0.27	0.29

753 * Values with an asterisk represent data at a confidence level greater than 95%.

754

755 **Table 4.** Correlation coefficients from linear regressions of visibility and different
 756 occurrence frequencies of rain amount type for all seasons.

Rain rate Season	Light rain	Moderate rain	Heavy rain	Very heavy rain	Rain amount
Spring	0.61*	0.51*	0.38*	0.08	0.67*
Summer	0.23	-0.13	-0.26	-0.44*	-0.04
Autumn	0.52*	0.18	0.25	-0.10	0.45*
Winter	0.55*	0.22	0.20	-0.05	0.49*

757 * Values with an asterisk represent data at a confidence level greater than 95%.

758

759

760

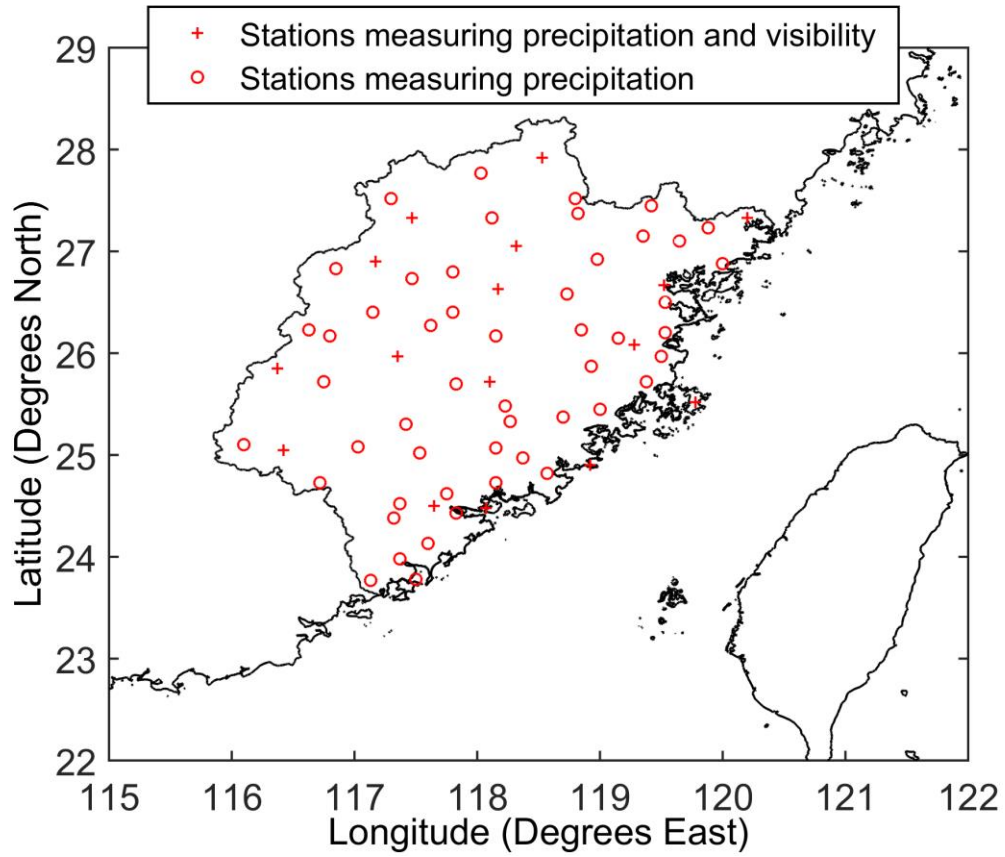
761

762

763

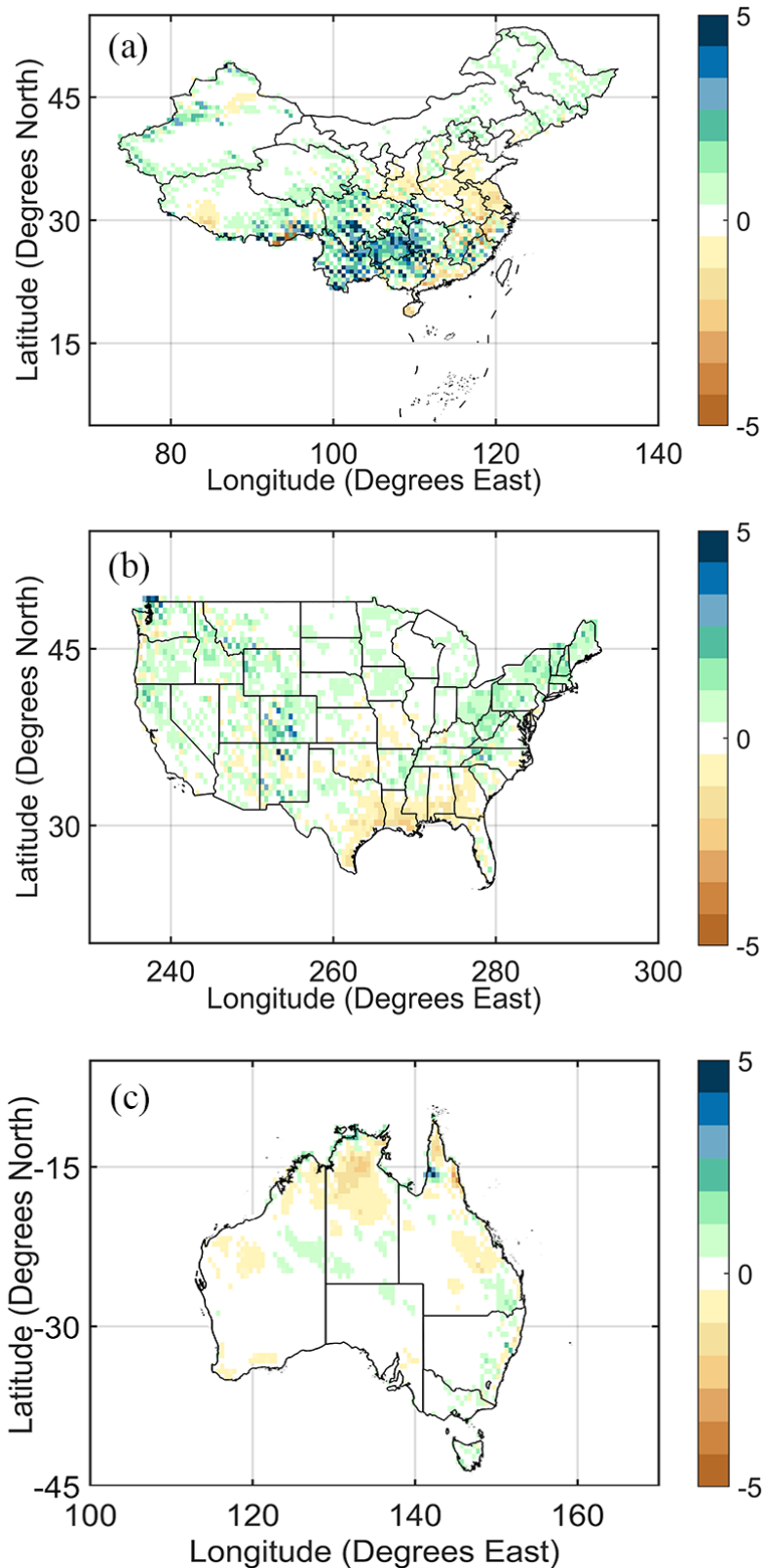
764

765



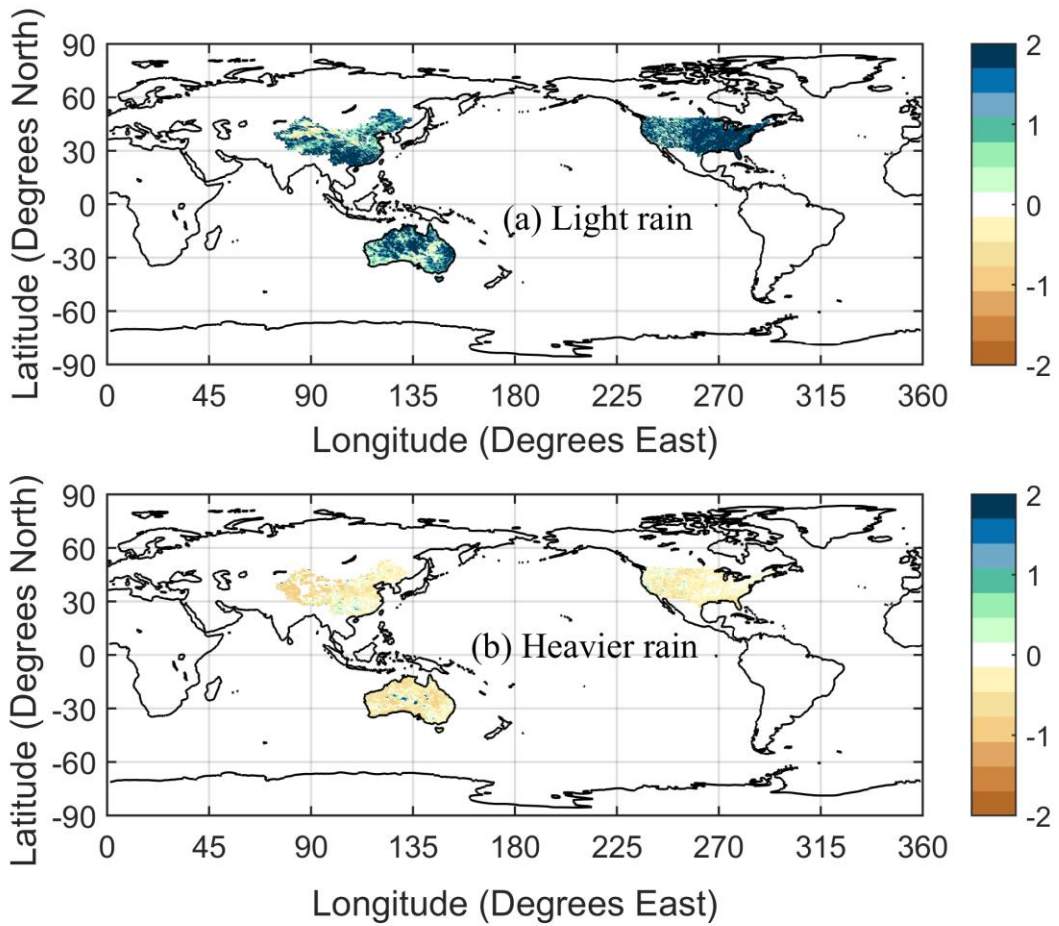
766

767 **Fig. 1.** Locations of 67 stations measuring precipitation in Fujian Province. Plus
 768 symbols show the locations of the 16 stations where visibility measurements are also
 769 made. This figure was plotted using the equidistant cylindrical projection.



770

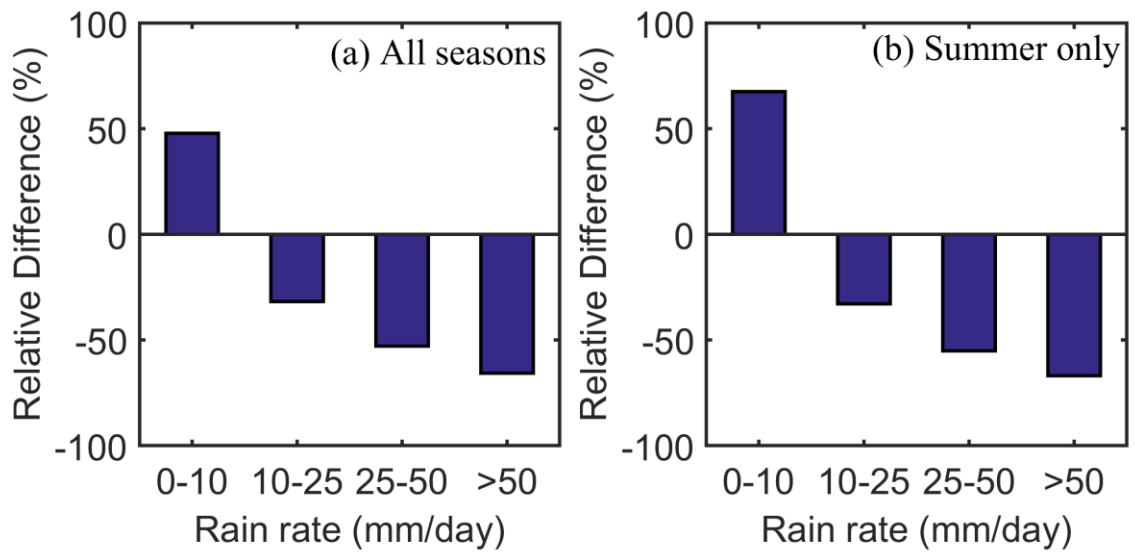
771 **Fig. 2.** Annual mean precipitation differences (in mm d⁻¹) between the GFS model
 772 forecast and the CPC analysis in three countries: (a) China, (b) the contiguous U.S.,
 773 and (c) Australia. Data are from the year 2015. This figure was plotted using the
 774 equidistant cylindrical projection.



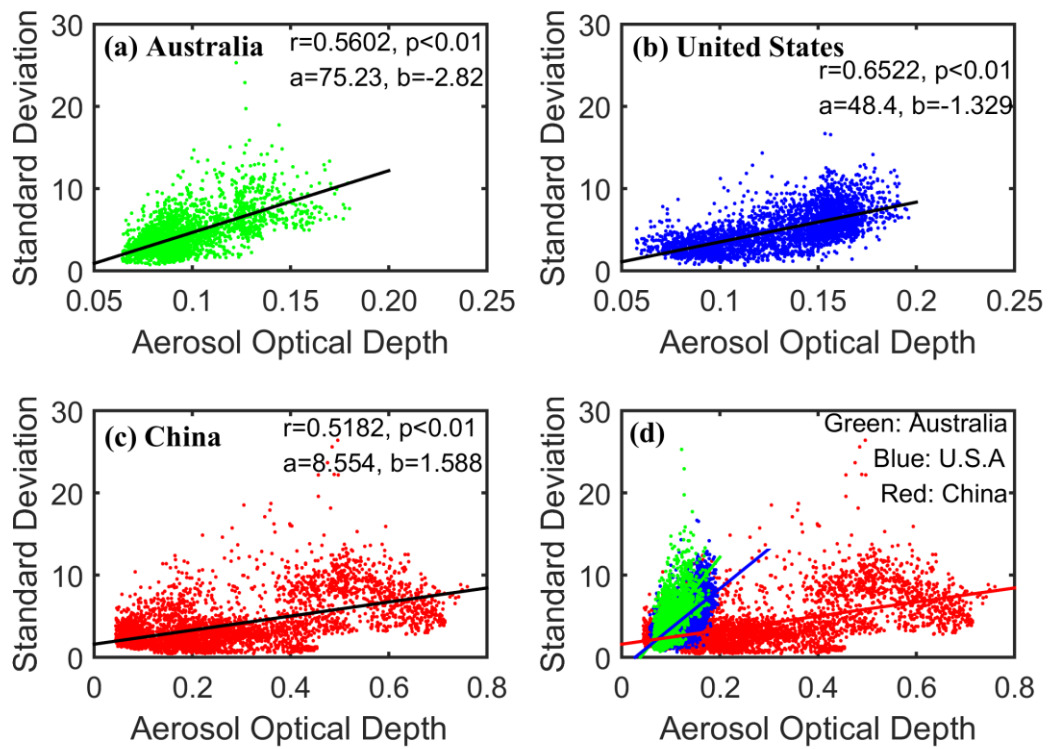
775

776 **Fig. 3.** Annual mean relative difference (in mm d^{-1}) between forecast and observed
 777 precipitation for (a) light rain ($< 10 \text{ mm d}^{-1}$) and (b) heavier rain ($> 10 \text{ mm d}^{-1}$). Data
 778 are from the year 2015. This figure was plotted using the equidistant cylindrical
 779 projection.

780



781
 782 **Fig. 4.** Mean relative difference in precipitation between forecast and observed daily
 783 light ($< 10 \text{ mm d}^{-1}$), moderate ($10\text{--}25 \text{ mm d}^{-1}$), heavy ($25\text{--}50 \text{ mm d}^{-1}$), and very heavy
 784 ($> 50 \text{ mm d}^{-1}$) rain amounts for (a) all seasons and (b) summer only. Data are from the
 785 year 2015 and from the three countries considered in the study.
 786

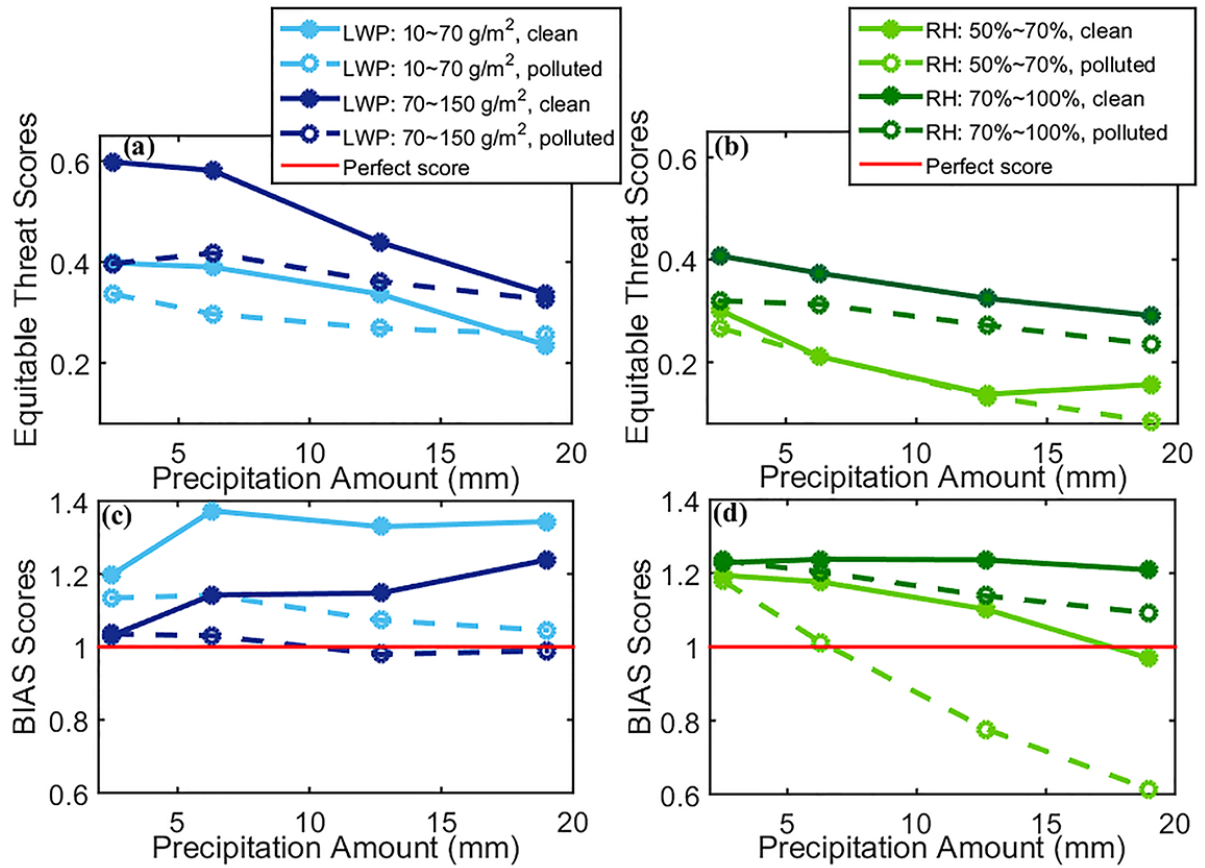


787

788 **Fig. 5.** Standard deviations of the daily precipitation difference as a function of
 789 aerosol optical depth for (a) Australia (green points), (b) the United States (blue
 790 points), (c) China (red points), and (d) all three countries. Data are from the year 2015.
 791 The slopes (a) and y-intercepts (b) of the best-fit lines through the data in (a) to (c) are
 792 given, as well as the correlation coefficients (r).
 793

794

795



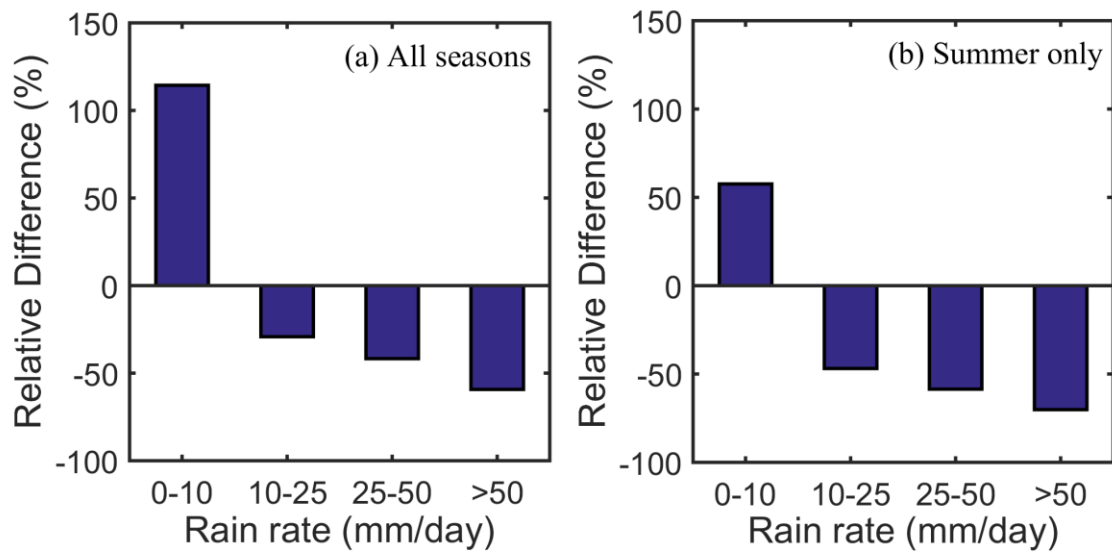
796

797

798 **Fig. 6.** Equitable threat scores (a, b) and bias (BIAS) scores (c, d) as a function of
799 precipitation amount for fixed ranges of liquid water path (LWP; a, c) and relative
800 humidity (RH; b, d) under clean and polluted conditions. The LWP is divided into two
801 categories: 10–70 g m⁻² (light blue) and 70–150 g m⁻² (dark blue). Data are from
802 August 2015 in the U.S, China, and Australia. The RH is divided into two categories:
803 50–70% (light green) and 70–100% (dark green). Data are from year 2015. For a
804 given LWP or RH condition, the top and bottom one-third of AOD values are defined
805 as polluted and clean subsets of data, respectively. The solid lines represent the clean
806 scenario and the dotted lines represent the polluted scenario. The horizontal red lines
807 in (c) and (d) represent perfect scores.

808

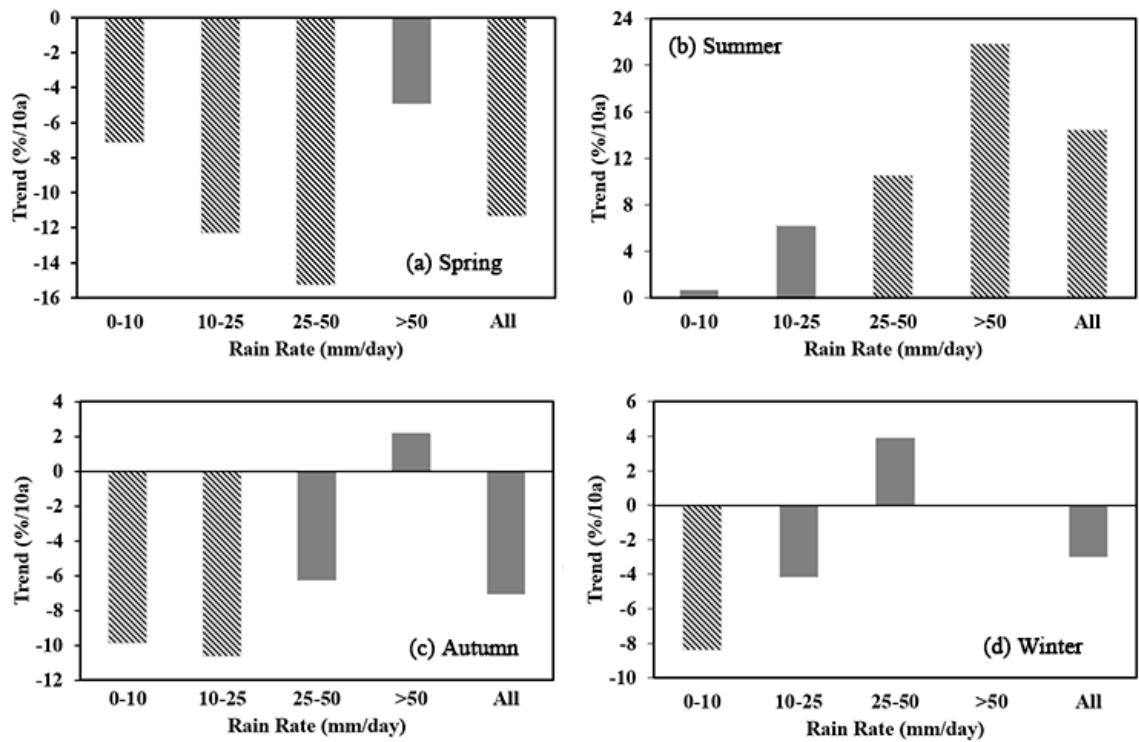
809



810

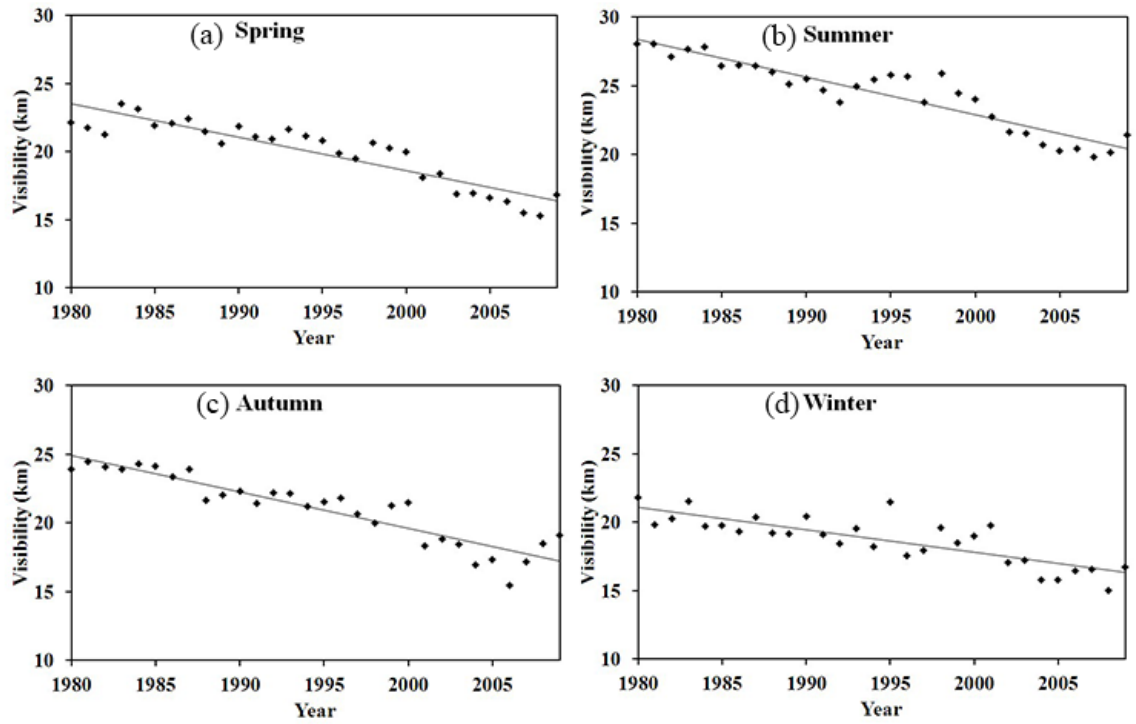
811 **Fig. 7.** Mean relative precipitation differences between forecast and observed daily
 812 light ($< 10 \text{ mm d}^{-1}$), moderate ($10\text{--}25 \text{ mm d}^{-1}$), heavy ($25\text{--}50 \text{ mm d}^{-1}$), and very heavy
 813 ($> 50 \text{ mm d}^{-1}$) rain amounts for (a) all seasons and (b) summer only in Fujian
 814 Province, China. Data are from 1985–2010.

815



817

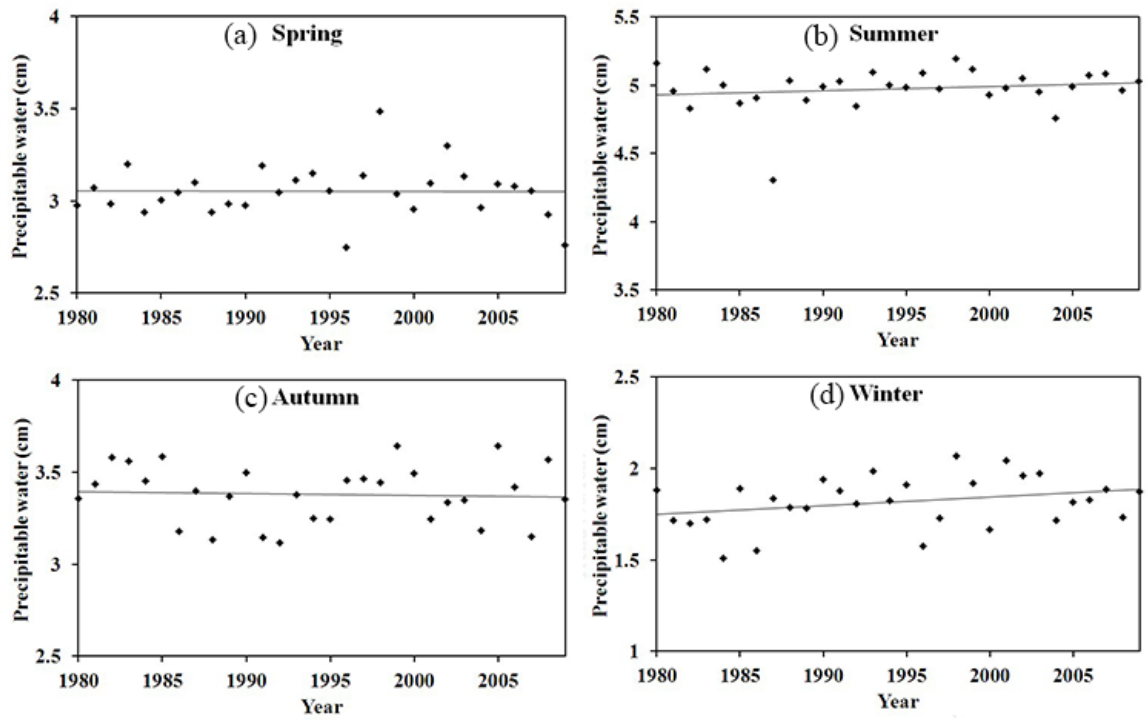
818 **Fig. 8.** Trends (percent change per decade) in mean daily light rain ($< 10 \text{ mm d}^{-1}$),
 819 moderate rain ($10\text{--}25 \text{ mm d}^{-1}$), heavy rain ($25\text{--}50 \text{ mm d}^{-1}$), very heavy rain ($> 50 \text{ mm}$
 820 d^{-1}), and total rain amounts for (a) spring, (b) summer, (c) autumn, and (d) winter in
 821 Fujian Province, China. Data are from 1980–2009. Cross-hatched bars represent data
 822 at a confidence level greater than 95%.



823

824 **Fig. 9.** Annual mean visibilities in (a) spring, (b) summer, (c) autumn, and (d) winter
 825 in Fujian Province, China. Data are from 1980–2009. Least squares regression lines at
 826 the 95% confidence level are shown.

827

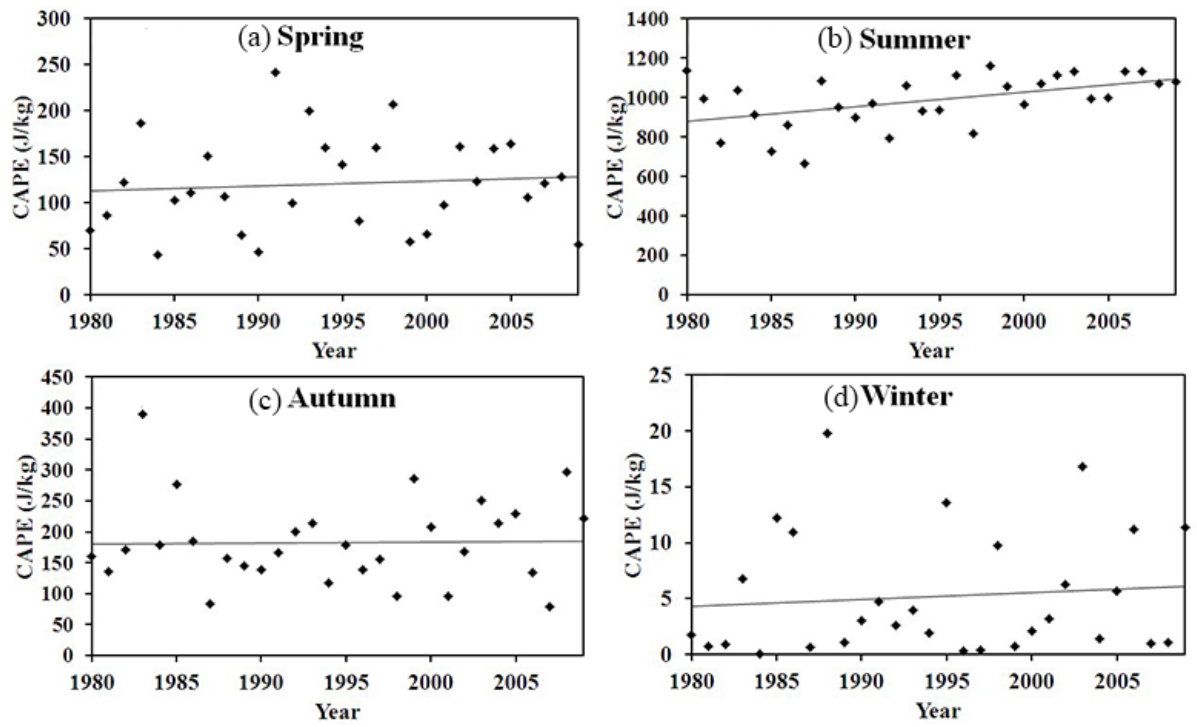


828

829 **Fig. 10.** Same as Fig. 9, except for precipitable water vapor.

830

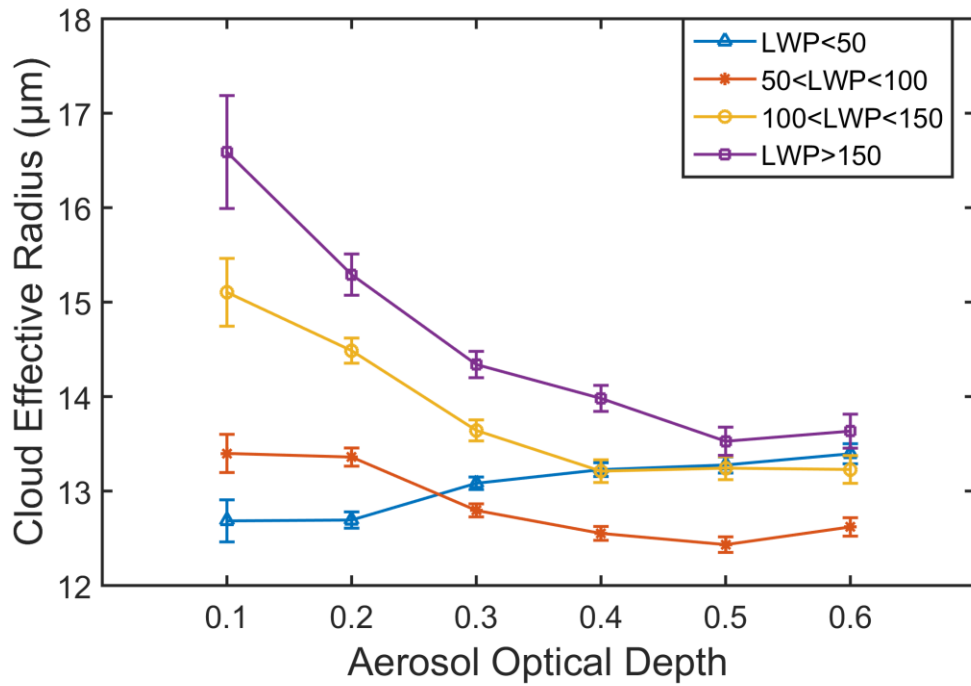
831



832

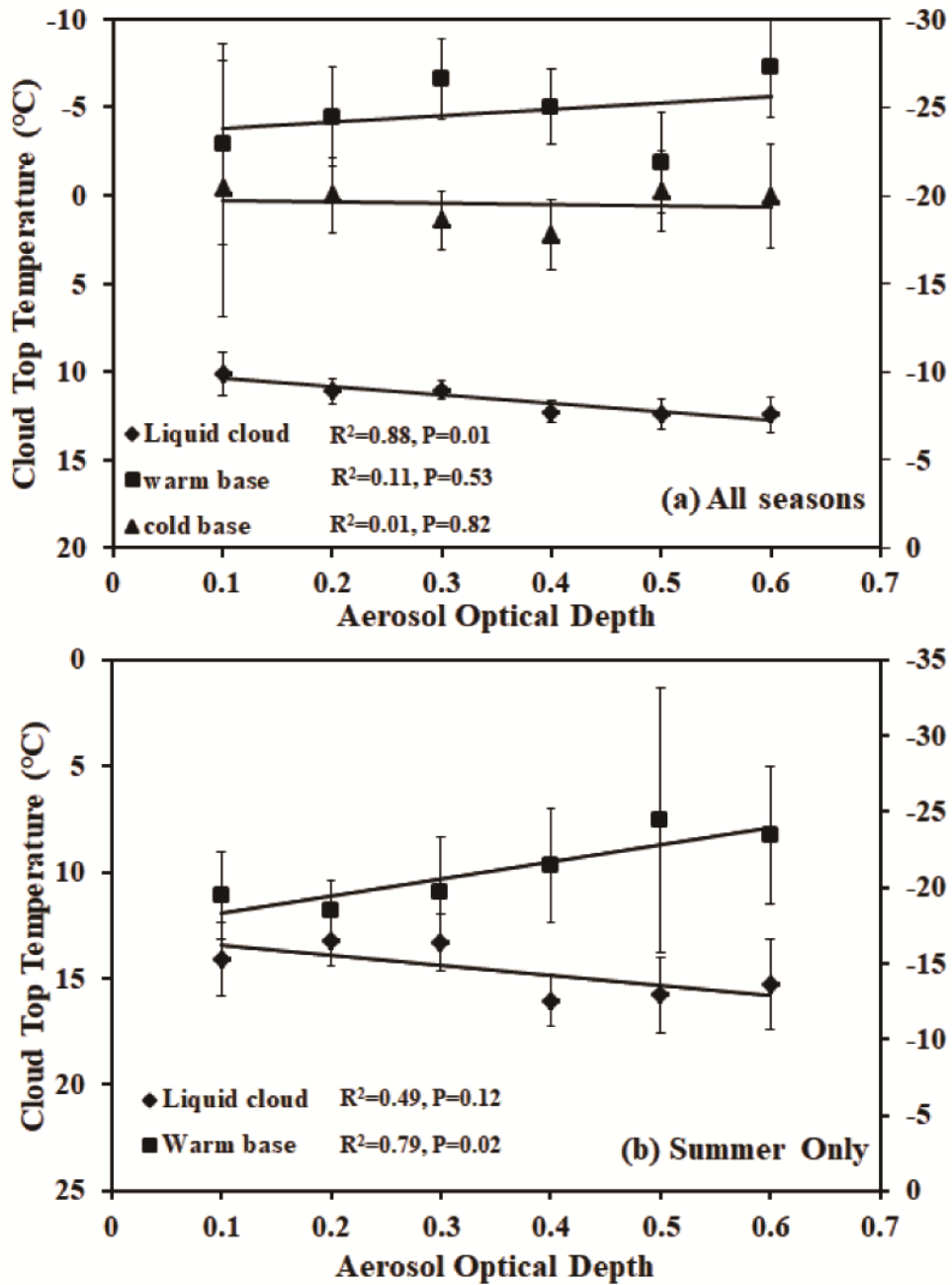
833 **Fig. 11.** Same as Fig. 9, except for convective available potential energy (CAPE).

834



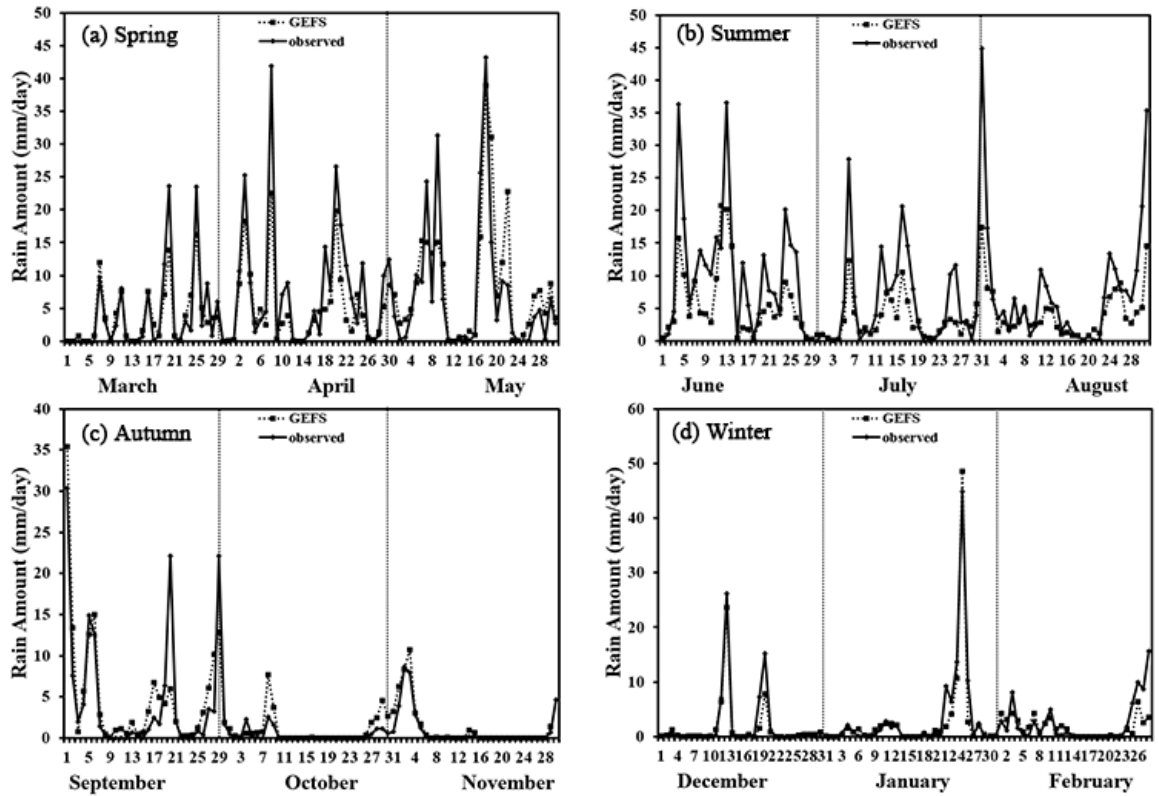
836

837 **Fig. 12.** Cloud effective radius as a function of aerosol optical depth for liquid clouds
 838 (clouds with top temperatures greater than 273 K) in Fujian Province, China. Blue
 839 triangles represent cases where the liquid water path (LWP) is less than 50 g m⁻²,
 840 orange stars represent LWPs between 50 g m⁻² and 100 g m⁻², yellow circles represent
 841 LWPs between 100 g m⁻² and 150 g m⁻², and purple squares represent LWPs greater
 842 than 150 g m⁻². Error bars represent one standard error. Data are from 2003–2012.



843

844 **Fig. 13.** Cloud-top temperature as a function of aerosol optical depth for (a) liquid,
 845 warm-base mixed-phase, and cold-base mixed-phase clouds in all seasons, and (b)
 846 liquid and warm-base mixed-phase clouds in summer in Fujian Province, China.
 847 Diamonds represent liquid clouds, squares represent warm-base mixed-phase clouds,
 848 and triangles represent cold-base mixed-phase clouds. Right-hand ordinates are for
 849 warm-base and cold-base mixed-phase clouds. Data are from 2006–2010.



850
851
852
853
854

Fig. 14. Time series of regionally-averaged daily rainfall amount in Fujian Province, China in (a) spring, (b) summer, (c) autumn, and (d) winter. Dotted lines represent rainfall forecasts from the Global Ensemble Forecast System and solid lines represent rainfall measurements from gauge-based observations. Data are from 2001.